Steroid assay. Tissue culture supernatant from Y-1 clones was assayed for fluorogenic steroid content as described[23], using corticosterone (Sigma) as standard.

Received 29 July; accepted 6 October 1997.

1. Zanaria, E. *et al.* An unusual member of the nuclear hormone receptor superfamily responsible for X-linked adrenal hypoplasia congenita. *Nature* **372,** 635–641 (1994).
2. Muscatelli, F. *et al.* Mutations in the *DAX-1* gene give rise to both X-linked adrenal hypoplasia congenita and hypoganadotropic hypogonadism. *Nature* **372,** 672–676 (1994).
3. Swain, A. *et al.* Mouse *Dax1* expression is consistent with a role in sex determination as well as in adrenal and hypothalamus function. *Nature Genet.* **12,** 404–409 (1996).
4. Ikeda, Y. *et al.* Steroidogenic factor 1 and Dax-1 colocalize in multiple cell lineages: Potential links in endocrine development. *Mol. Endocrinol.* **10,** 1261–1272 (1996).
5. Tamai, K. T. *et al.* Hormonal and developmental regulation of DAX-1 expression in Sertoli cells. *Mol. Endocrinol.* **10,** 1561–1569 (1996).
6. Laudet, V., Stehelin, D. & Clevers, H. Ancestry and diversity of the HMG box superfamily. *Nucleic Acids Res.* **21,** 2493–2501 (1993).
7. Weir, H. M. *et al.* Structure of the HMG box motif in the B-domain of HMG-1. *EMBO J.* **12,** 1311–1319 (1993).
8. Bianchi, M. E., Beltrame, M. & Paonessa, G. Specific recognition of cruciform DNA by nuclear protein HMG1. *Science* **243,** 1056–1059 (1989).
9. Werner, M. H., Gronenborn, A. M. & Clore, M. G. Intercalation, DNA kinking, and the control of transcription. *Science* **271,** 778–784 (1996).
10. Stocco, D. M. & Clark, B. J. Regulation of the acute production of steroids in steroidogenic cells. *Endocr. Rev.* **17,** 221–244 (1996).
11. Clark, B. J., Wells, J., King, S. R. & Stocco, D. M. The purification, cloning and expression of a novel luteinizing hormone-induced mitochondrial protein in MA-10 mouse Leydig tumor cells. *J. Biol. Chem.* **269,** 28314–28322 (1994).
12. Lin, D. *et al.* Role of steroidogenic acute regulatory protein in adrenal and gonadal steroidogenesis. *Science* **267,** 1828–1831 (1995).
13. Palecek, E. Local supercoil-stabilized DNA structures. *Crit. Rev. Biochem. Mol. Biol.* **26,** 151–226 (1991).
14. Sugawara, T. *et al.* Structure of the human steroidogenic acute regulatory protein (StAR) gene: StAR stimualtes mitochondrial cholesterol 27-hydroxylase activity. *Biochemsitry* **34,** 12506–12512 (1995).
15. Lalli, E. *et al.* A transcriptional silencing domain in DAX-1 whose mutation causes adrenal hypoplasia congenita. *Mol. Endocrinol.* (in the press).
16. Schimmer, B. P. Adrenocortical Y1 cells. *Meth. Enzymol.* **58,** 570–574 (1979).
17. Bose, H. S., Sugawara, T., Strauss, J. F. II & Miller, W. L. The pathophysiology and genetics of congenital lipoid adrenal hyperplasia. *N. Engl. J. Med.* **335,** 1870–1878 (1996).
18. Caron, K. M. *et al.* Characterization of the promoter region of the mouse gene encoding the steroidogenic acute regulatory protein. *Mol. Endocrinol.* **11,** 138–147 (1997).
19. Sugawara, T., Holt, J. A., Kiriakidou, M. & Strauss, J. F. III Steroidogenic factor 1-dependent promoter activity of the human steroidogenic acute regulatory protein (StAR)(gene. *Biochemistry* **35,** 9052–9059 (1996).
20. Sinclair, A. H. *et al.* A gene from the human sex-determining region encodes a protein with homology to a conserved DNA-binding motif. *Nature* **346,** 240–244 (1990).
21. Bardoni, B. *et al.* A dosage sensitive locus at chromosome Xp21 is involved in male to female sex reversal. *Nature Genet.* **7,** 497–501 (1994).
22. Ito, M., Yu, R. & Jameson, J. L. DAX-1 inhibits SF-1-mediated transactivation via a carboxy-terminal domain that is deleted in adrenal hypoplasia congenita. *Mol. Cell. Biol.* **17,** 1476–1483 (1997).
23. Clegg, C. H., Correll, L. A., Cadd, G. G. & McKnight, G. S. Inhibition of intracellular cAMP-dependent protein kinase using mutant genes of the regulatory type I subunit. *J. Biol. Chem.* **262,** 13111–13119 (1987).
24. Foulkes, N. S., Borrelli, E. & Sassone-Corsi, P. CREM gene: Use of alternative DNA binding domains generates multiple antagonists of cAMP-induced transcription. *Cell* **64,** 739–749 (1991).
25. Laoide, B. M., Foulkes, N. S., Schlotter, F. & Sassone-Corsi, P. The functional versatility of CREM is determined by its modular structure. *EMBO J.* **12,** 1179–1191 (1993).

Acknowledgements. We thank E. Remboutsika, M. Lamas, B. Bardoni, J. F. Strauss III, K. L. Parker, G. Camerino and E. Borrelli for help, discussions, and gifts of material, and E. Heitz, Y. Lutz, B. Boulay and S. Metz for technical assistance. E.Z. is an EEC postdoctoral fellow; E.L. was supported by a Telethon Italy Fellowship. This study was funded by grants from the NIH (to D.M.S.) and from CNRS, INSERM, Centre Hôspitalier Universitaire Régional, FRM, Rhône-Poulenc Rorer (Bioavenir) and ARC (P.S.-C.).

Correspondence and requests for materials should be addressed to P.S.-C. (e-mail: paolosc@igbmc.u.-strasbg.fr).

corrections

The optical counterpart of the isolated neutron star RX J185635–3754

Frederick M. Walter & Lynn D. Matthews

Nature **389,** 358–360 (1997)

There was a typographical error in the declination of the optical counterpart given at the start of the fourth paragraph: this should be $-37^\circ 54' 35.8''$. □

Imaging of radiocarbon-labelled tracer molecules in neural tissue using accelerator mass spectrometry

R. E. M. Hedges, Z. X. Jiang, C. Bronk Ramsey, A. Cowey, J. D. B. Roberts & P. Somogyi

Nature **383,** 823–826 (1996)

We regret that we did not refer in this Letter to two publications[1,2]. These authors showed that scanning SIMS (rather than SIAMS) can be used in a similar way to image tracers, including ^{14}C, in tissue. We had not appreciated, from the published data, the extent to which the performance of the instrument might be equivalent to that of SIAMS. □

1. Slodzian, G., Diagne, B., Girard, F., Boust, F. & Hillion, F. Scanning secondary ion analytical microscopy with parallel detection. *Biology of the Cell* **74,** 43–50 (1992).
2. Hindié, E., Coulomb, B., Beaupin, R. & Galle, P. Mapping the cellular distribution of labelled molecules by SIMS microscopy. *Biology of the Cell* **74,** 82–88 (1992).

Structure of the inhibitory receptor for human natural killer cells resembles haematopoietic receptors

Qing R. Fan, Lidia Mosyak, Christine C. Winter, Nicolai Wagtmann, Eric O. Long & Don C. Wiley

Nature **389,** 96–100 (1997)

The sixth sentence in the introductory bold paragraph should read: "The human p58 natural killer-cell inhibitory receptor clone 42 recognizes HLA-Cw4, -Cw2, -Cw5 and -Cw6, but not HLA-Cw3, -Cw1, -Cw7 or -Cw8, which are recognized by p58 killer-cell inhibitory receptor clone 43 (ref. 3)." □

Crystal structures of fragment D from human fibrinogen and its crosslinked counterpart from fibrin

Glen Spraggon, Stephen J. Everse & Russell F. Doolittle

Nature **389,** 455–462 (1997)

In a sentence on page 459 describing the orientation of the Gly-Pro-Arg-Pro-amide ligand as bound to the double-D fragment, the wrong aspartate was referred to on one occasion. The sentence should have read: "…the α-amino group being juxtaposed between the residues Aspγ364 and Aspγ330, and the guanidino group of the arginine lying between the carboxyl group of Aspγ330 and the carboxamide of Glnγ329 (Fig. 5a, b)." □

Nature © Macmillan Publishers Ltd 1997

The optical counterpart of the isolated neutron star RX J185635–3754

Frederick M. Walter & Lynn D. Matthews

Department of Physics and Astronomy, Z=3800, State University of New York, Stony Brook, New York 11794-3800, USA

The extreme densities[1] of neutron stars make them an ideal system in which to investigate the equation of state of nuclear matter; accurate determinations of neutron star masses and radii are crucial for this. Current observations of neutron stars in binary systems yield masses that are generally consistent with theory[2]. But measurements of radii are more difficult as they require the detection of thermal radiation from the surface, which in general is masked by emission from non-thermal processes in radio pulsars[3] and X-ray binary systems[4]. Isolated radio-quiet neutron stars[5] offer the best opportunity to observe the surface thermal emission. Here we report the detection of the optical counterpart of a candidate isolated neutron star, RX J185635–3754 (ref. 6). Our optical flux data, combined with existing extreme ultraviolet[7] and X-ray[6] observations, show the spectrum to be approximately thermal. By adopting the upper bound to the distance of the source, and assuming a plausible model for the spectral energy distribution, we find that the radius of the object cannot exceed 14 km. This result is inconsistent with a number of recent equations of state[8] proposed for neutron stars.

RX J185635–3754 lies along a line of sight to the R CrA molecular cloud, which itself is only 130 pc away[9]; X-ray observations indicate that it must lie in front of the molecular cloud[10], as the column of absorbing material is too small to include a molecular cloud. No optical counterpart had been found to a limiting magnitude of $V \approx 24$ (refs 6, 11, 12), which yields an X-ray-to-optical flux ratio $f_X/f_V > 7{,}000$. Such an extreme ratio rules out most objects other than neutron stars as possible sources[6].

The observations were made with the Hubble Space Telescope (HST) Wide Field and Planetary Camera 2 (WFPC2). They consist of a dithered pair of images through the F606W filter, totalling 4,400 s, and a single 2,400-s image in the F300W filter. The fully reduced images are shown in Fig. 1.

We identify the blue object at right ascension 18 h 56 min 35.41 s, declination −37° 54′ 8″ (J2000) as the optical counterpart. This position is referred to the reference frame of the Digital Sky Survey, by measuring the positions of stars in common between the two images. The offset (HST − DSS) is +0.065 s, −1.1″. The object lies 3.9 arcsec from the originally published X-ray position[6], but only 2.0 arcsec from the revised position[11], which used a more accurate boresight correction. The formal uncertainty on the position is less than ±0.02 arcsec, but we estimate that there may be uncertainties of up to 2.0 arcsec in the transformation to the DSS reference frame. The object has a stellar point spread function in each filter. The identification as the X-ray source counterpart is based on the blue colour of the object.

We determined the fluxes using aperture photometry. We measured the flux within an aperture of selectable size, and the background with an aperture of 40 pixels radius, with an inner radius 3 pixels outside the source extraction radius. The background was iteratively filtered to exclude points >3 standard deviations (s.d.) from the mean before computing the background level. We measured the source counts within a 9-pixel (0.41-arcsec) radius circle, and corrected to a 1-arcsec aperture using the measured point spread function of bright sources in the image. The flux in the F606W filter $f_{606} = 1.58 \pm 0.39 \times 10^{-19}$ erg cm^{-2} s^{-1}Å^{-1}; the flux in the F300W filter $f_{606} = 1.63 \pm 0.38 \times 10^{-18}$ erg cm^{-2} s^{-1}Å^{-1}. The main uncertainties in the fluxes are due to the Poisson noise in the background. The target is detected with a signal-to-noise ratio >8 in each band. On the Space Telescope (ST) magnitude system[13], the f_{606} and f_{300} magnitudes are 25.9 and 23.4, respectively; f_{606} corresponds to a magnitude of 25.6 on the Vega magnitude system[13], and f_X/f_V about 75,000. The $f_{300} - f_{606}$ colour is −2.5 on the ST magnitude system (an infinitely hot black body has an $f_{300} - f_{606}$ colour of −3.0 in this system).

The magnitudes are consistent with the identification as a

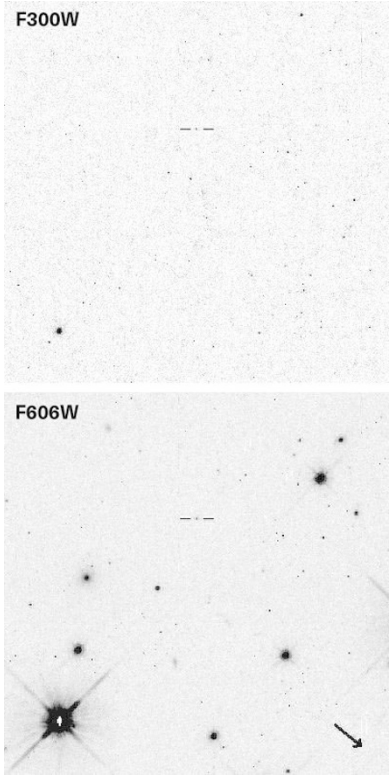

Figure 1 The central 400 × 400 pixels (17.5 × 17.5 arcsec) of the planetary camera images. The optical counterpart is marked. The arrow at the lower right of the F606W image points north. The bright star to the lower left is star F; star J is near the tail of the arrow. Both images are heavily stretched to bring out the faint features. The data were reduced using the WFPC2 team reduction method, which includes application of a high signal-to-noise superdark frame composed of dark frames taken as near as possible in time to the data of the observations, as well as an updated warm-pixel correction for highly time-dependent dark current by using a delta (local) dark frame[20]. All images were processed by CR-SPLIT to facilitate cosmic-ray removal. The CR-SPLIT exposures were co-added using the VISTA PICCRS package. Final cosmic ray identification was done by blinking the split exposures in each filter. Residual cosmic rays were hand-cleaned only in the vicinity of the neutron star; they are evident elsewhere in the images. The dithered F606W frames were co-added using a simple adaptation of the Fruchter and Hook 'drizzling' algorithm[21] written by A. M. Watson; we used 2 × 2 oversampling and a drop size of 1 × 1 oversampled pixels. F606W and F300W magnitudes of stars identified by Walter *et al.*[6] (letters) and Campana *et al.*[12] (numbers) are: C, (–, 19.4); D, (–, 20.9); F, (–, 19.0); I, (18.7, 21.3); J, (20.8, 23.3), L, (–, 18.9); 21, (20.9, 24.6); 23, (23.6, 23.6); 24, (20.2, 22.9); 28, (21.4, >25). Stars C, D, F and L have saturated pixels in the F606W image.

Nature © Macmillan Publishers Ltd 1997

neutron star. The hot white dwarf Hz43 has about three times the X-ray flux of RX J185635–3754 and a comparably blue colour ($U-V=-1.2$), but at $V=12.8$, f_X/f_V is close to unity. A lightly reddened hot white dwarf at $V=25.6$ would lie at a distance of about 50 kpc. The counterpart must be much smaller than a white dwarf if it is foreground to the molecular cloud.

Little, if any, of the ultraviolet flux can be due to a red leak in the F300W filter. The reddest star, number 21 (ref. 12), has $f_{300}/f_{606}=0.04$. We take this as the maximum possible red leak. As the neutron star candidate is considerably bluer than all the other stars, with $f_{300}/f_{606}=10$, any red leak must be negligible.

If the object is a hot black body, the intrinsic f_{300}/f_{606} flux ratio is the ratio of the fourth power of the wavelengths, and the visual extinction $A_V=0.52^{+0.13}_{-0.20}$ mag, using the Seaton[14] extinction curve with $R=3.1$. This is 2.3σ deviant from the measured X-ray absorption column of $1.4\pm0.1\times10^{20}\,\mathrm{cm}^{-2}$ ($A_V=0.07$ mag), and might suggest the existence of spectral features in the optical spectrum. We note that excess emission near 6,000 Å is seen in the spectrum of isolated pulsars[15,16], but at much larger contrast. This emission could be attributable either to non-thermal emission from a magnetosphere or line emission from a surrounding nebula[17]; spectroscopic observations will be needed to characterize this excess.

The spectral energy distribution (SED) is shown in Fig. 2. We utilize the Rosat Position Sensitive Proportional Counter (PSPC) and High Resolution Imager data[6], the EUVE Scanner count rate[7], and the two optical points. The black-body fit to the X-ray data underpredicts the optical flux by a factor of 2.4 ± 0.5 at 3,000 Å and a factor of 3.7 ± 0.9 at 6,060 Å. This is evidence that the spectrum is more complex than a simple black body. Models with two black-body components, or more sophisticated models with surface temperature variations[18], can match the f_{300} flux. Models involving radiative transfer through H, He or non-magnetic Fe atmospheres[19] fail to predict the optical fluxes.

The blue colour and the reasonably close agreement of the optical fluxes with the extrapolated X-ray flux confirms that this object is the optical counterpart of the X-ray source. The isolated nature of the object, the approximately thermal character of its emission and the lack of strong variability on any timescale suggest that we are seeing the surface emission from a nearby neutron star. This is the only non-pulsating, single neutron star confirmed so far. As such, this object affords a unique opportunity to study the surface of a neutron star, and to study the interior equation of state. If the emission from the surface is truly thermal, then one can determine the angular diameter of the star. The radius follows from the parallax. Not knowing the distance, we can estimate upper limits to the radius by assuming that the neutron star is foreground to the R CrA molecular cloud.

The $kT_\infty=57$ eV X-ray black body[6] yields a radius as seen at infinity, $R_\infty<8$ km. The models with more complex surface temperature distributions yield larger values for the radius. These models have more free parameters, including the inclinations of the rotation and magnetic poles to the line of sight and the functional form of the surface temperature distribution. A full analysis of these models is under way (P. An, J. M. Lattimer, F. M. W. and M. Prakash, manuscript in preparation). Here we illustrate that a simple model with the magnetic and rotation axes approximately co-aligned and in the plane of the sky (consistent with the lack of strong modulation of the X-ray flux) can match the observed SED. The temperature is assumed to vary as $(\mathrm{latitude})^{0.25}$ (ref. 18). The polar cap temperature is 62 eV. This model SED, shown in Fig. 2, has $R_\infty<14$ km, for a distance <130 pc.

Although RX J185635–3754 offers the cleanest example now known of the surface of an isolated neutron star, there are significant unknowns. Although the upper limit to the distance is reasonably certain, the true distance is not known. Planned observations with the HST will permit us to measure the parallax and determine a firm lower limit of $R_\infty>8(D/130\mathrm{pc})$ km, where D is the distance in parsecs. Estimates of the radius are model-dependent and hence require a better understanding of the SED at all wavelengths. Planned X-ray and optical observations will define the SED better, and will indicate how much, if any, of the optical excess above a black body can be due to non-thermal emission processes. Assuming the latitudinally varying surface temperature model[18], we find $R_\infty=14(D/130\mathrm{pc})$ km. This permits us to exclude most conventional equations of state[8] (for mass $>0.5\,M_\odot$) if $D<100$ pc. Similarly, for mass $>1\,M_\odot$, we can rule out equations of state incorporating kaon condensates[8] if D is less than ~75 pc. We expect that further observations of RX J185635–3754 will yield important insights into the nature of the surfaces and the interior equation of state of neutron stars. □

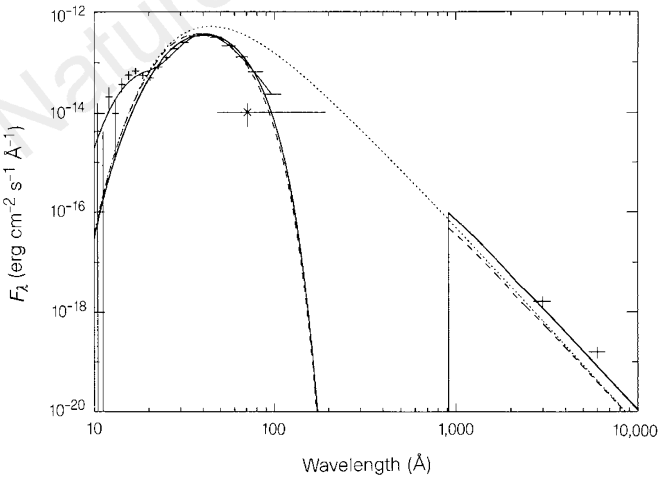

Figure 2 The spectral energy distribution of RX J185635–3754. The Rosat PSPC data[6], the EUVE scanner flux[7] and the two fluxes from the HST are plotted with error bars. The thin line is the black-body fit to the Rosat PSPC data, including the broadening effects of the instrumental response function. The dotted line is the unreddened 57 eV black body; the broken line is the black-body fit reddened by $A_V=0.07$ mag (the gap between ~200 and 912 Å is due to absorption in the interstellar medium). The thick solid line is a reddened model with a sinusoidal temperature variation over the surface[18] ($T_{\mathrm{pole}}=62$ eV; $T_{\mathrm{equator}}=0$). The f_{300} and f_{606} fluxes exceed those predicted by these simple models.

Received 7 April; accepted 24 July 1997.

1. Baym, G. & Pethick, C. Physics of neutron stars. *Annu. Rev. Astron. Astrophys.* **17,** 415–443 (1979).
2. van Paradijs, J. & McClintock, J. E. in *X-Ray Binaries* (eds Lewin, W. H. G., van Paradijs, J. & van den Heuvel, E. P. J.) 58–125 (Cambridge Univ. Press, 1995).
3. Phinney, E. S. & Kulkarni, S. R. Binary and millisecond pulsars. *Annu. Rev. Astron. Astrophys.* **32,** 591–639 (1994).
4. White, N. E., Nagase, F. & Parmar, A. N. in *X-Ray Binaries* (eds Lewin, W. H. G., van Paradijs, J. & van den Heuvel, E. P. J.) 1–57 (Cambridge Univ. Press, 1995).
5. Carraveo, P. A., Bignami, G. F. & Trümper, J. Radio-silent isolated neutron stars as a new astronomical reality. *Astron. Astrophys. Rev.* **7,** 209–216 (1996).
6. Walter, F. M., Wolk, S. J. & Neuhäuser, R. Discovery of a nearby isolated neutron star. *Nature* **379,** 233–235 (1996).
7. Lampton, M. *et al.* An all-sky catalog of faint Extreme Ultraviolet sources. *Astrophys. J. Suppl.* **108,** 545–557 (1997).
8. Prakash, M. & Lattimer, J. M. The radius of the neutron star RX J185635-3754 and implications for the equation of state. *Astrophys. J. Lett.* (submitted).
9. Marraco, H. G. & Rydgren, A. E. On the distance and membership of the R CrA T association. *Astron. J.* **86,** 62–68 (1981).
10. Wang, Q. D. in *The Soft X-Ray Cosmos* (AIP Conference Proceedings 313) (eds Schlegel, E. M. & Petre, R.) 301–305 (AIP, New York, 1994).
11. Neuhäuser, R., Thomas, H.-C., Danner, R., Peschke, S. & Walter, F. M. On the X-ray position and deep optical imaging of the neutron star candidate RXJ1856.5-3754. *Astron. Astrophys.* **318,** L43–L46 (1996).
12. Campana, S., Mereghetti, S. & Sidoli, L. Is RXJ1856.5-3754 an old neutron star? *Astron. Astrophys.* **320,** 783–786 (1997).
13. Leitherer, C. (ed.) *HST Data Handbook* (Space Telescope Science Inst., Baltimore, 1995).
14. Seaton, M. Interstellar extinction in the UV. *Mon. Not. R. Astron. Soc.* **187,** 73P–76P (1979).
15. Bignami, G. F., Caraveo, P. A., Mignani, R., Edelstein, J. & Bowyer, S. Multiwavelength data suggest cyclotron feature on the hot thermal continuum of Geminga. *Astrophys. J. Lett.* **456,** L111–L114 (1996).
16. Pavlov, G. G., Stringfellow, G. S. & Córdova, F. A. Hubble Space Telescope observations of pulsars. *Astrophys. J.* **467,** 370–384 (1996).
17. Blaes, O., Warren, O. & Madau, P. Accreting, isolated neutron stars: III. Preheating of infalling gas and cometary H II regions. *Astrophys. J.* **454,** 370–381 (1995).

Nature © Macmillan Publishers Ltd 1997

18. Greenstein, G. & Hartke, G. J. Pulselike character of blackbody radiation from neutron stars. *Astrophys. J.* **271,** 283–293 (1983).
19. Pavlov, G. G., Zavlin, V., Trümper, J. & Neuhäuser, R. Multiwavelength observations of isolated neutron stars as a tool to prove the properties of their surfaces. *Astrophys. J. Lett.* **472,** L33–L36 (1996).
20. Holtzman, J. A. *et al*. The photometric performance and calibration of WFPC2. *Pub. Astron. Soc. Pacif.* **107,** 1065–1093 (1995).
21. Fruchter, A. S. & Hook, R. N. in *The Hubble Space Telescope and the High Redshift Universe* (eds Tanvir, N. R., Salamanca, A. & Wall, J. V.) (World Scientific, Singapore, 1997).

Acknowledgements. We thank A. M. Watson for performing the bulk of the image reduction, and J. Holtzman for peparing and providing the delta dark and superdark frames necessary for our data; we also thank them both for their time and patience in the discussion of data reduction issues. We acknowledge useful discussions with P. An, J. Lattimer and R. Neuhäuser.

Correspondence and requests for materials should be addressed to F.M.W. (e-mail: fwalter@astro.sunysb.edu).

A general boundary condition for liquid flow at solid surfaces

Peter A. Thompson* & Sandra M. Troian†

** The Celerity Group, 20 Nassau Street, Suite 209, Princeton, New Jersey 08542, USA*
† Department of Chemical Engineering, Princeton University, Princeton, New Jersey 08544, USA

Modelling fluid flows past a surface is a general problem in science and engineering, and requires some assumption about the nature of the fluid motion (the boundary condition) at the solid interface. One of the simplest boundary conditions is the no-slip condition[1,2], which dictates that a liquid element adjacent to the surface assumes the velocity of the surface. Although this condition has been remarkably successful in reproducing the characteristics of many types of flow, there exist situations in which it leads to singular or unrealistic behaviour—for example, the spreading of a liquid on a solid substrate[3–8], corner flow[9,10] and the extrusion of polymer melts from a capillary tube[11–13]. Numerous boundary conditions that allow for finite slip at the solid interface have been used to rectify these difficulties[4,5,11,13,14]. But these phenomenological models fail to provide a universal picture of the momentum transport that occurs at liquid/solid interfaces. Here we present results from molecular dynamics simulations of newtonian liquids under shear which indicate that there exists a general nonlinear relationship between the amount of slip and the local shear rate at a solid surface. The boundary condition is controlled by the extent to which the liquid 'feels' corrugations in the surface energy of the solid (owing in the present case to the atomic close-packing). Our generalized boundary condition allows us to relate the degree of slip to the underlying static properties and dynamic interactions of the walls and the fluid.

During the past decade molecular dynamics simulations have emerged as a powerful tool for probing the microscopic behaviour of liquids at interfaces (ref. 15, and references therein). Studies have demonstrated how solids induce order in adjacent liquids and how this order, in turn, controls the amount of momentum transfer[16]. The no-slip condition has been shown to be just one of many allowable flow boundary conditions ranging from pure slip to multi-layer locking. The degree of slip at the boundary depends on a number of interfacial parameters including the strength of the liquid–solid coupling, the thermal roughness of the interface, and the commensurability of wall and liquid densities[16]. These findings have led to a new understanding of stick-slip phenomena in boundary lubrication[17] and have revealed the sensitivity of liquid spreading to microstructure at the liquid/solid interface[7,8]. Earlier work[16] investigated flows in a regime for which the degree of slip was independent of local shear rate $\dot{\gamma}$. This regime is described by the well-known linear Navier boundary condition[1] in which $\Delta V = L_s\dot{\gamma}$, where ΔV is the velocity difference between the solid and adjacent liquid, and L_s is a constant slip length. Here we examine the

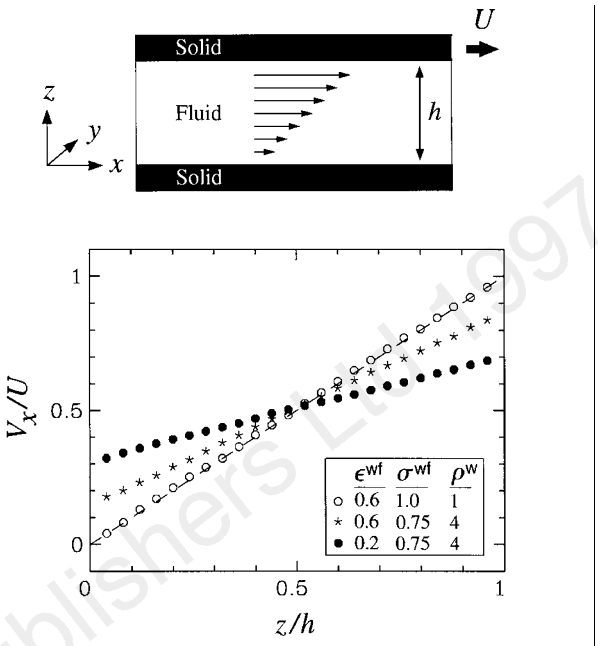

Figure 1 Steady-state flow profiles and schematic of the Couette flow geometry. The Couette cell measured $12.51\sigma \times 7.22\sigma \times h$ where h varied from 16.71σ to 24.57σ. The number of fluid molecules ranged from 1,152 to 1,728, respectively. The $\hat{\mathbf{x}}$-direction of the cell is aligned along the $[11\bar{2}]$ orientation of the face-centred cubic lattice comprising the wall, and periodic boundary conditions are imposed along $\hat{\mathbf{x}}$ and $\hat{\mathbf{y}}$. The flow profiles were obtained for systems with $U = 1.0\sigma\tau^{-1}$, $h = 24.57\sigma$, and walls characterized by the indicated density and Lennard–Jones parameters. Values for ϵ^{wf}, σ^{wf} and ρ^{w} (see text) are in units of ϵ, σ and ρ, respectively. Following an equilibration period of $\sim 100\tau$, the profiles were computed by averaging the instantaneous particle velocities within bins of width $\sim 1\sigma$ spanning the distance between the two walls. The duration of the averaging varied from 250τ to $7{,}000\tau$ depending on the signal-to-noise ratio. Accurate resolution of flows with $\dot{\gamma} < 0.01\tau^{-1}$ typically required $>2{,}500\tau$ of averaging. The dashed line indicates Couette flow with a no-slip boundary condition.

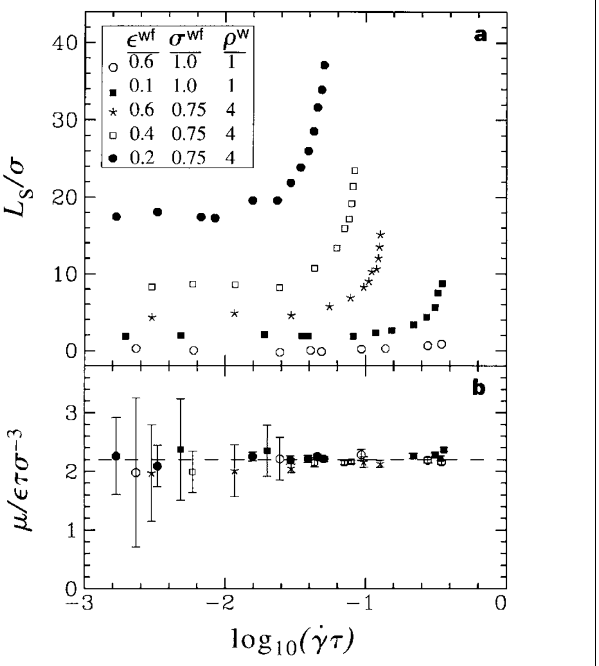

Figure 2 Variation of the slip length L_s (panel **a**) and viscosity μ (panel **b**) as a function of shear rate for systems with the indicated interfacial properties. L_s was computed from the definition $L_s = \Delta V_x/\dot{\gamma}$, which for Couette flow reduces to $(U/\dot{\gamma} - h)/2$: μ was computed from the relation $\mu = P_{zx}/\dot{\gamma}$, where P_{zx} is the zx-component of the microscopic stress tensor averaged across the cell[19].

Nature © Macmillan Publishers Ltd 1997

Acknowledgements. We thank S. Endow for the GST–MC5 clone; M. McNiven for the MMR48 antibody; M. Fritz for the rhodamine-labelled tubulin; U. Euteneuer, H. Felgner, R. Gräf and S. Linder for advice; and S. Fuchs for technical assistance. This work was supported by a Graduiertenkolleg fellowship to U.H. and a grant from the DFG to M.S.

Correspondence and requests for materials should be addressed to M.S. (e-mail: schliwa@bio.med.uni-muenchen.de).

Structure of the inhibitory receptor for human natural killer cells resembles haematopoietic receptors

Qing R. Fan*†, Lidia Mosyak*†, Christine C. Winter‡, Nicolai Wagtmann‡, Eric O. Long‡ & Don C. Wiley*

** Department of Molecular and Cellular Biology, Howard Hughes Medical Institute, Harvard University, 7 Divinity Avenue, Cambridge, Massachusetts 02138, USA*
‡ Laboratory of Immunogenetics, National Institute of Allergy and Infectious Diseases, National Institutes of Health, 12441 Parklawn Drive, Rockville, Maryland 20852, USA
† These authors contributed equally to this work.

Abnormal cells deficient in class I major histocompatibility complex (MHC) expression are lysed by a class of lymphocytes called natural killer (NK) cells[1]. This lysis provides a defence against pathogens and tumour cells that downregulate MHC expression to avoid an MHC-restricted, T-cell immune response. Normal cells escape lysis because their MHC molecules are recognized by NK-cell inhibitory receptors, which inhibit lysis[2]. Several such inhibitory receptor families have been described in humans and mice (reviewed in ref. 2). In the human killer-cell inhibitory receptor family, individual p58 members are specific for a subset of class I human leukocyte antigen (HLA)-C molecules. The human p58 natural killer-cell inhibitory receptor clone 42 recognizes HLA-Cw4, -Cw2 and -Cw6, but not HLA-Cw3, -Cw2, -Cw7 or -Cw8, which are recognized by p58 killer-cell inhibitor receptor clone 43 (ref. 3). We have determined the X-ray structure of the p58 NK-cell inhibitory receptor clone 42 at 1.7-Å resolution. The structure has tandem immunoglobulin-like domains positioned at an acute, 60-degree angle. Loops on the outside of the elbow between the domains form a binding site projected away from the NK-cell surface. The topology of the domains and their arrangement relative to each other reveal a relationship to the haematopoietic receptor family, with implications for the signalling mechanism in NK cells.

The soluble ectodomain of the p58 natural killer-cell inhibitory receptor (KIR) that we crystallized was expressed in bacteria and refolded *in vitro*[4]. It specifically blocks the binding of a KIR–immunoglobulin fusion protein to cells expressing HLA-Cw4, but has no effect on the binding of a KIR–immunoglobulin fusion protein specific for HLA-CW3 to cells expressing HLA-CW3 (ref. 4). The entire KIR ectodomain, residues 1–224, and a shorter form, residues 1–200, without the stem domain of 24 residues, were both shown by a gel-shift assay to bind to soluble, recombinant HLA-Cw4 (ref. 4). As predicted from sequence similarity[5], the overall fold of each KIR domain resembles immunoglobulin-like domains containing two antiparallel β-sheets[6] (Fig. 1a, b). Topologically, the p58 KIR structure has tandem fibronectin type III-like domains, which are structurally similar to immunoglobulin domains. The two domains are equal in size (domain D1, residues 6–101; domain D2, residues 105–200), and are connected by a three-residue linker (residues 102–104) (Fig. 1b).

The topology of the D1 immunoglobulin-like domain is of the h-type[6], similar to that of the D1 domains of the human growth hormone receptor (hGHR)[7], human prolactin receptor (hPLR)[7], and the erythropoietin receptor (EPOR)[8]. The D2 domain has the closely related s-type topology[6] found in the D2 domains of hGHR, hPLR and EPOR[8–10], and both domains of class II receptors of the haematopoietic superfamily, including the α-chain of the interferon-γ receptor (IFN-γRα)[11], and tissue factor[12,13]. The s-type topology has also been found in other two-domain structures, including the co-receptor CD4 (refs 14, 15), the cell-adhesion molecule CD2 (ref. 16) and neuroglian[17]. However, in both CD2 and CD4, the s-type domain is paired in tandem with a variable-type immunoglobulin domain and the two domains assume a linear conformation, lacking the elbow region found in all of the haematopoietic receptors and KIR. Although some members of the haematopoietic receptor superfamily contain additional domains, ligand binding is mediated through the h- or s-type domains[7]. The s-type topology of D2 has a β-sheet of three strands, A, B and E (Fig. 1a, b, dark orange) packed against a β-sheet of four strands, C′, C, F and G (Fig. 1a, b, light orange). In h-type topology of the D1 domain, the C′ strand is elongated, pairing first with the C strand of the C′CFG β-sheet and at its far end (where it is renamed D) pairing with the E strand of the ABE(D) β-sheet (Fig. 1a, b). The switch from one β-sheet to the other occurs at a kink in strand C′/D at Gly 53. When superimposed, the D1 and D2 domains, which have 40% sequence identity, are strikingly similar in structure with a root-mean-square (r.m.s.) deviation of 0.9 Å for 85 Cα pairs.

Table 1 Statistics for data collection and refinement

Data collection

Data set	Wavelength (Å)	Scattering factors (e)		Resolution (Å)	Unique reflections	Average $I/\sigma(I)$	Completeness (%)	R_{sym} (%)†
		f′	*f″*					
MAD	0.9639 (remote)	–3.49	3.72	10.0–2.2	11,480	18.9	98.7 (99.1)	7.3 (11.7)
	0.9791 (peak	–7.89	4.72	10.0–2.2	11,449	18.5	98.6 (99.1)	7.2 (11.6)
	0.9794 (edge)	–9.86	3.05	10.0–2.2	11,495	18.8	98.8 (99.1)	7.0 (11.3)
native	0.918			16.0–1.7	25,065	17.1	99.5 (97.8)	7.3 (23.4)

Refinement (6–1.7 Å)

R_{cryst} (R_{free})‡ (%)	Reflections (free)	Non-hydrogen protein atoms	solvent molecules	R.m.s. deviations		
				Bonds (Å)	Angles (°)	*B*-factors (Å²)
20.5 (25.5)	24,473 (2,427)	1,513	211	0.010	1.83	2.85

Values in parentheses correspond to the last resolution shell; 2.28–2.20 Å for MAD data sets, or 1.76–1.70 Å for native data set.
* The values of *f′* and *f″* for λ_{peak} and λ_{edge} were derived from the experimental values of the absorption spectrum; values for λ_{remote} were calculated form theoretical cross-sections[30].
† $R_{sym} = \Sigma |I_i - \langle I \rangle| / \Sigma I_i$, where I_i is the intensity of an individual reflection, and $\langle I \rangle$ is the average intensity of that reflection. Bijvöet mates were considered as separate reflections.
‡ $R_{cryst} = \Sigma \big| |F_p| - |F_c| \big| / \Sigma |F_p|$, where F_c is the calculated structure factor. R_{free} is equivalent to R_{cryst}, but calculated for a randomly chosen 10% of reflections that were omitted from the refinement process.

Nature © Macmillan Publishers Ltd 1997

KIR domains define a new topological subtype[6], which we call Kh- and Ks-type, in which the carboxy-terminal half of strand A, named A′, pairs with strand G to form a five-stranded sheet C′CFGA′ (Fig. 1a, b, light orange) by switching at *cis* prolines (residues 14 and 114) from one β-sheet to another, as found in variable domains of antibody light chains, CD8 and T-cell antigen receptors.

A signature sequence motif of class I haematopoietic receptors, the WSXWS box[18], is also present in p58 KIR. The p58 clone 42 KIR (p58-cl42) contains at residues 188–192 a variant of the WSXWS sequence motif (WSKSS) in D2, in the same location as found in the haematopoietic receptor family (Fig. 1a, b). Like the motif in the other structures, the WSKSS sequence in KIR assumes a polyproline type II conformation, resulting in a wide β-bulge[8–10] in which the hydroxyl groups of the two conserved serine residues (underlined) form hydrogen bonds to the adjacent F-strand backbone, replacing the usual backbone-to-backbone hydrogen bonds between strands in a β-sheet. A surface cluster of aromatic and charged side chains near the motif present in several haematopoietic receptors[8–10] is absent in KIR. KIR differs from members of the haematopoietic receptor superfamily in that a variant of the motif also occurs in D1 (Fig. 1a, b). The sequence VSAPS, residues 90–94, forms the same type of β-bulge at the homologous position. Variants of both the V SAPS and WSKSS sequences are found in the sequences of all KIR immunoglobulin-like domains, with the two structurally important serines completely conserved.

Helical linkers of at least four residues in length have been found linking the D1 and D2 domains in five members of the haematopoietic receptor family: hGHR, hPLR, EPOR, IFN-γRα and tissue factor[8–13]. The D1 and D2 domains of the KIR are more tightly connected by a three-residue linker (residues 102–104) with a helical conformation ($\phi = -95.7$ deg, $\psi = -18.4$ deg) at Leu 104.

Most of the side chains in the D1–D2 interface are conserved in all KIR sequences, and the few differences there are appear consistent with the observed packing, suggesting that the V shape will be a feature of all p58 and p70 KIRs. Extensive hydrogen bonding between strands of both domains and the large buried solvent-accessible surface area, 1,076 Å^2 (calculated using the program SURFACE[19]; probe radius 1.4 Å), suggest that the elbow angle is fixed. The D1–D2 interface includes a three-stranded parallel β-sheet formed by the two strands A′ and G from the D1 domain and a short segment of strand G in the D2 domain (Fig. 1a, b). D1–D2 contacts occur not only at the tip of the V (Fig. 2a, black) but also across the gap between the arms of the V (Fig. 2a, red). Most of the polar interactions found at the interface involve main-chain atoms, and are therefore independent of sequence variation.

Site-directed mutations indicate strongly that the binding site on

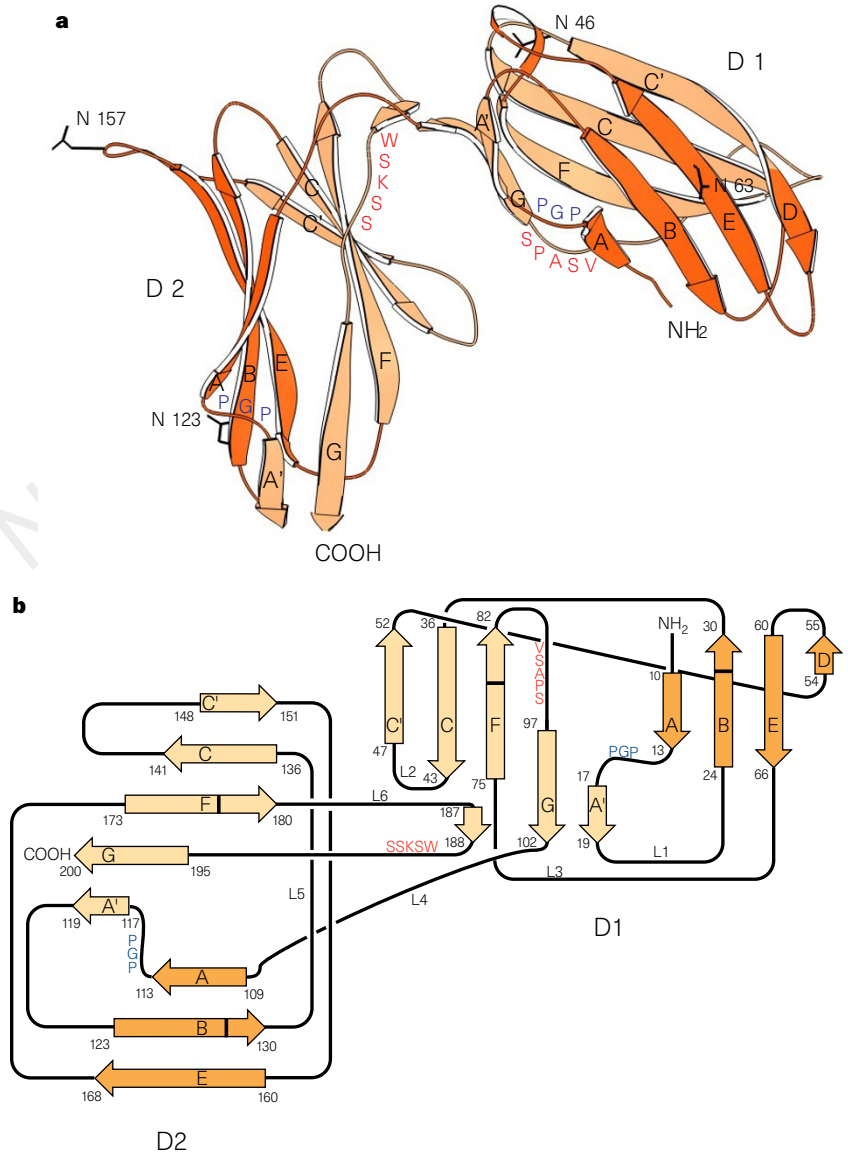

Figure 1 Structure and topology of p58-cl42 KIR. **a**, KIR domain D1 is N-terminal, and D2 is C-terminal; ABED β-sheet (dark orange) and C′CFGA′β-sheet (light orange); WSKSS and VSAPS motifs (red); potential glycosylation sites at asparagines 46, 63, 123 and 157 (black). **b**, Topological diagram showing the h-type immunoglobulin-like fold of D1 and the s-type fold of D2. The β-sheet at the D1–D2 interface (strands A′ and G in D1 and a fragment of strand G in D2) is shown below D1. Loops L1–L6 are implicated in ligand binding by the haematopoietic receptors, hGHR, hPLR and EPOR. Cysteines 28, 79, 128 and 177 are indicated by black bars.

Nature © Macmillan Publishers Ltd 1997

p58-cl42 for its HLA ligand includes Met 44 (ref. 20) on the C–C′ loop that projects from the elbow between D1 and D2 (Fig. 2b, red star; Fig. 1b, L2). Exchanging Met 44 in p58-cl42 with lysine, found at that position in p58-cl43, switched the specificity of p58-cl42 from HLA-Cw4 to HLA-Cw3, and vice versa[20]. Of the six ligand-binding loops of class I haematopoietic receptors (L1–L6 in Fig. 1b), sequence variation among KIRs (Fig. 2b) implicates at least three in ligand binding (L2, L3 and L6 in Fig. 1b). Loops at the elbow between domains contact ligand in the 1 : 1 complex of human prolactin receptor (hPLR) (Fig. 3c, green) with growth hormone (hGH) (orange).

In contrast to the 'elbow angles' found in the haematopoietic receptors, which are 90 deg for hGHR, EPOR and hPLR and 120 deg for IFN-γRα and tissue factor, the interdomain angle in KIR is 60 deg (compare Fig. 3a, b). The KIRs may thus define a new structural class of receptors, related to the haematopoietic receptor family that binds soluble ligands, but adapted, through the acute interdomain angle, to bind to membrane-bound ligands during cell–cell interactions that result in signalling.

The KIR binding site on class I MHC molecules has been mapped to the α1 domain (reviewed in ref. 2). Residues in the region of the C-terminal end of the α1-domain α helix, and on the loop following it in the sequence (Fig. 3e, red), have been identified as part of the site on HLA-C and HLA-B molecules recognized by p58 and p70 KIRs. The inhibitory signal delivered by KIR after binding an MHC molecule is initiated by the phosphorylation of its cytoplasmic ITIM motif which, in turn, binds to the Src-homology 2 (SH2) domains of the tyrosine phosphatase SHP-1, thereby both recruiting it to the membrane and revealing its phosphatase activity[21,22]. This mechanism requires the recruitment of a protein tyrosine kinase to phosphorylate the KIR ITIM following KIR–MHC binding.

By analogy to the haematopoietic receptors, KIR signalling following ligand binding might be expected to involve either dimerization of KIR or binding to another polypeptide chain[7,23]. Formation of a homodimer would be expected to bring the cytoplasmic domains of KIR into close proximity, which may facilitate phosphorylation of the ITIM motif by a cytoplasmic kinase, as in the case of the hGHR and EPOR[23]. Alternatively, formation of a heterodimer of KIR with another polypeptide that contains an associated kinase (covalently or non-covalently linked) could lead directly to phosphorylation of the KIR ITIM, as in the case of the interleukin (IL)-3/granulocyte macrophage colony-stimulating factor/IL-5 and IL-6 receptors[23]. It is possible that after binding an MHC molecule, a p58 KIR may heterodimerize with a p50 form of the KIR family, which, because of their potential to deliver positive signals[24], might be able to recruit a tyrosine kinase to the ITIM of an HLA-bound p58-KIR.

By analogy to hGHR and EPOR (Fig. 3d), dimerization of KIR might be expected to involve pairing of D2 domains (shown schematically in Fig. 3e). Disulphide-linked dimers have been observed in one group of p70 KIR[25] that are probably linked through a cysteine corresponding to position 220 in the p58 KIR stem segment following D2, which favours dimerization through D2. The existence of preformed p70 KIR dimer before ligand binding

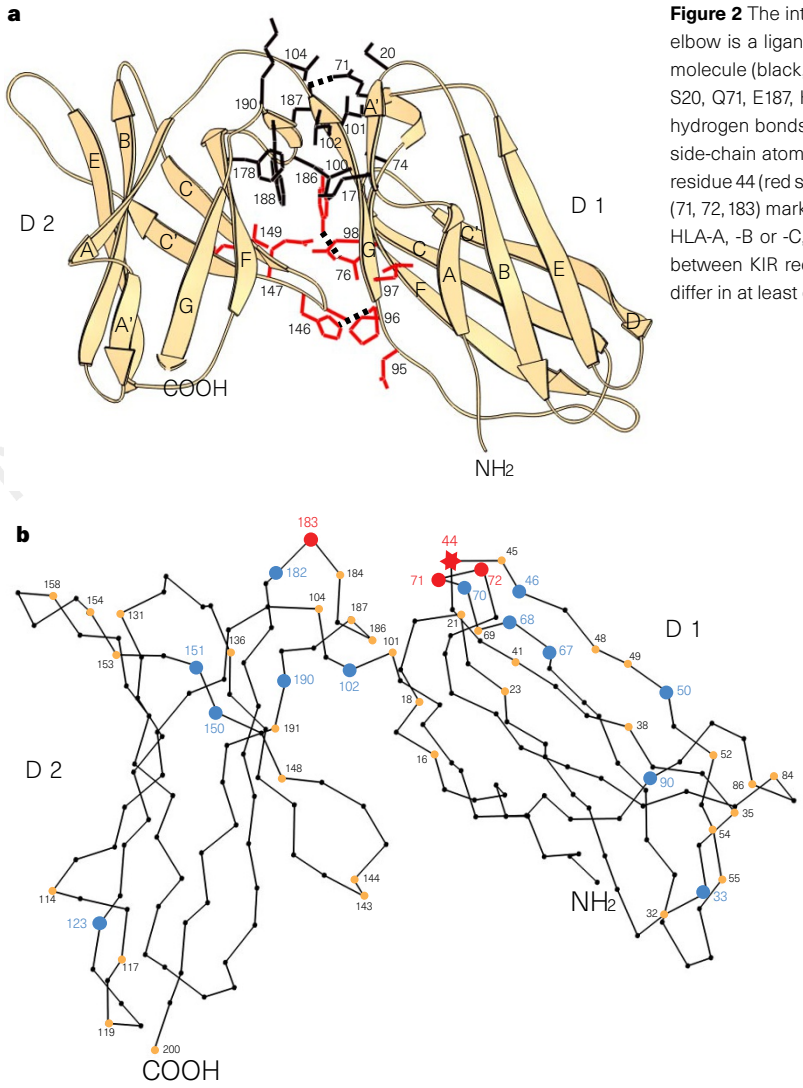

Figure 2 The interdomain interface defines a 60-deg angle and the interdomain elbow is a ligand-binding site. **a**, Non-polar contacts at the tip of the V-shaped molecule (black, V100, I102, L17, P178, W188, A74, I101, I104 and aliphatic parts of S20, Q71, E187, K190) and across the arms of the V (red). Of the 11 interdomain hydrogen bonds, 8 include β-sheet main-chain atoms (not shown); 3 use some side-chain atoms (P96–H146, Y186–T76, E187–N71; dotted lines). **b**, Exchanging residue 44 (red star) changes the specificity from HLA-Cw4 to HLA-Cw3. Red dots (71, 72, 183) mark positions that are conserved within subsets of KIR recognizing HLA-A, -B or -C, but are different in each KIR subset. Blue dots mark variation between KIR recognizing HLA-Cw4 and HLA-Cw3. Positions with orange dots differ in at least one KIR sequence.

Nature © Macmillan Publishers Ltd 1997

indicates that the signalling mechanism, at least of that KIR, may involve molecules other than a putative receptor dimer. The stem region of KIR may contribute to HLA binding (Q.R.F. *et al.*, unpublished data). The full ectodomain of p58-cl42 KIR (residues 1–224) completely blocked the binding of the shorter form (residues 1–200 lacking the stem segment) to soluble HLA-Cw4 on band-shift assays (data not shown). Furthermore, binding of the shorter form to HLA-Cw4 was reversed upon addition of the longer form, suggesting a higher dissociation constant for the complex between HLA-Cw4 and the shorter form. The more favourable binding observed between HLA-Cw4 and the KIR that includes the stem (residues 220–224) suggests a role for the C-terminal stem in ligand binding, possibly by stabilizing dimerization (Fig. 3e), considering the distance between the C terminus and the ligand-binding site (Fig. 2b).

The second receptor polypeptide chain that we postulate may bind in either a homodimer or heterodimer to a KIR–MHC complex (Fig. 3e) is expected, by analogy to the haematopoietic receptors: to have a much lower affinity for HLA, and bind only after the first KIR has bound; to bind to a second, as-yet undiscovered, site on MHC molecules; and to interact with the first KIR polypeptide at some as-yet undiscovered site, probably in the D2 domain. In the haematopoietic receptors, the affinity of the second receptor chain to the single-receptor/ligand complex is 500- to 1,000-fold weaker than the first, making detection and characterization of the second binding sites difficult[7]. This may account for the current lack of evidence for KIR dimerization by MHC molecules. □

Methods

Incorporation of Se-Met. The selenomethionyl (Se-Met) p58-cl42 KIR (residues 1–200) was expressed in *Escherichia coli* as inclusion bodies, refolded by dilution, and purified following the same procedure as native p58-cl42 (ref. 4). The incorporation of Se-Met was achieved by growing the cells in minimal medium (M9) supplemented with 2 mM $MgSO_4$, 0.1 mM $CaCl_2$, 0.2% glucose, 0.00005% thiamine, and 40 mg l^{-1} each of all L-amino acids except Cys and Met, and inducing the cells in the presence of 120 mg l^{-1} of Se-Met along with 100 mg l^{-1} each of Thr, Lys and Phe, and 50 mg l^{-1} each of Leu, Ile and Val. All

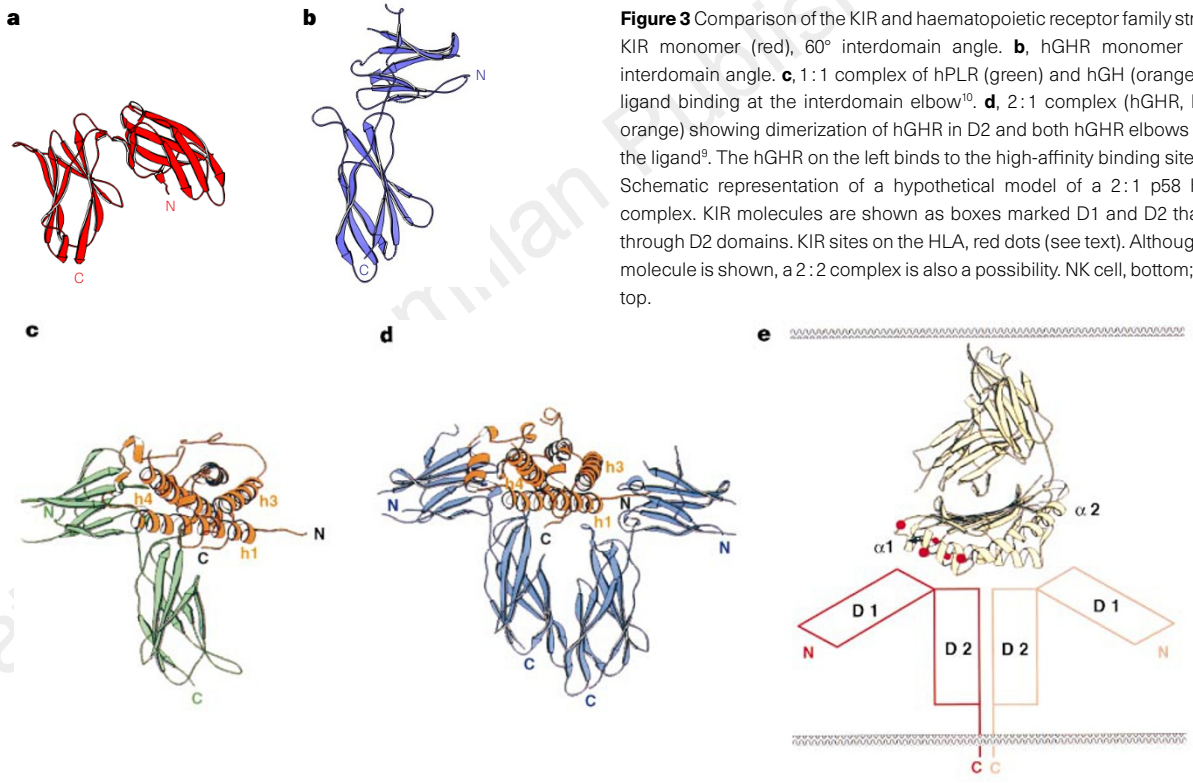

Figure 3 Comparison of the KIR and haematopoietic receptor family structures. **a**, KIR monomer (red), 60° interdomain angle. **b**, hGHR monomer (blue), 90° interdomain angle. **c**, 1:1 complex of hPLR (green) and hGH (orange), showing ligand binding at the interdomain elbow[10]. **d**, 2:1 complex (hGHR, blue; hGH, orange) showing dimerization of hGHR in D2 and both hGHR elbows contacting the ligand[9]. The hGHR on the left binds to the high-affinity binding site of hGH. **e**, Schematic representation of a hypothetical model of a 2:1 p58 KIR/HLA-C complex. KIR molecules are shown as boxes marked D1 and D2 that dimerize through D2 domains. KIR sites on the HLA, red dots (see text). Although one HLA molecule is shown, a 2:2 complex is also a possibility. NK cell, bottom; target cell, top.

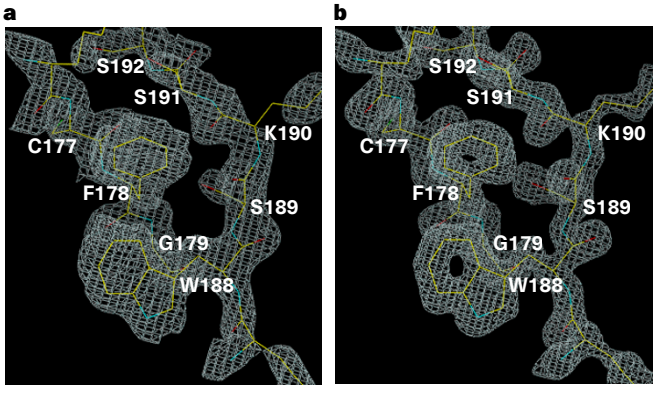

Figure 4 Electron-density maps showing the refined model in the region of the WSKSS sequence. **a**, A 2.2-Å resolution Fourier map calculated with MAD phases improved by density modification. **b**, A 1.7-Å resolution simulated-annealing-omit map calculated with the $2F_{obs} - F_{calc}$ amplitudes and model phases. Both maps are contoured at 1.2 σ level.

Nature © Macmillan Publishers Ltd 1997

five Met were substituted with Se-Met as determined by mass spectrometry.

Crystallization. Crystals of p58-cl42 were grown from 0.55 M $(NH_4)_2HPO_4$, 50 mM sodium citrate, pH 5.4, final pH 7.7. Hexagonal rods ($0.1 \times 0.1 \times 1.5\,mm^3$; space group $P6_1$; $a = b = 92.4$ Å, $c = 46.8$ Å; 1 molecule per asymmetric unit) grow two weeks after seeding. Se-met p58 crystallized under the same condition using the native crystals as seeds; the difference in cell dimensions was less than 0.5%. After the crystals were stabilized for at least 10 h in a harvesting solution (1.5 M $(NH_4)_2HPO_4$, 50 mM sodium citrate, pH 5.4, final pH 7.7), they were soaked for 2–5 min in a cryo-protecting solution (1.5 M $(NH_4)_2HPO_4$, 50 mM Na citrate, pH 5.4, 25% glycerol, final pH 7.7), and flash-cooled with liquid nitrogen.

Data collection. Multiwavelength anomalous dispersion (MAD)[26] data were collected to 2.2 Å with a 300-mm diameter MAR Research image-plate system at the X25 beamline of the National Synchrotron Light Source, Brookhaven National Laboratory. A high-resolution native data set was collected to 1.7 Å on the Princeton 2K CCD detector at F-1 beamline of the Cornell High Energy Synchrotron Source (CHESS). Data were processed (Table 1) using DENZO and SCALEPACK (HKL Research). Most of the subsequent processing used the CCP4 programs[19].

MAD phasing. MAD phasing was treated as a case of multiple isomorphous replacement[27]. Four selenium sites were identified from anomalous and dispersive difference Pattersons and were checked by difference Fouriers. The N-terminal methionine was disordered. Refinement of anomalous scatterer parameters and phase calculation were performed with MLPHARE[28]. Because of discrepancies between phasing statistics generated by MLPHARE and other programs[27], electron-density maps before and after model refinement are displayed instead of experimental phasing statistics (Fig. 4). The initial MAD map was improved by density modification using DM[19], assuming 40% solvent content. The correct space-group enantiomer $P6_1$ was identified by the presence of clear solvent boundary in the 2.2-Å electron-density maps.

Model refinement. The experimental MAD phases were used with the native data set to calculate the electron density for the native structure. Both density-modified and unmodified electron-density maps were used to build an 85% complete model with O (DATAONO AB). For refinement, data with $|F_{obs}| > 0$ were included. The model was initially refined at 10–2.2 Å using positional refinement and simulated annealing protocols in X-PLOR[29]. Several cycles of manual refitting and subsequent inclusion of lower-resolution data to 16 Å combined with bulk solvent correction allowed the missing loop regions to be traced. The resolution was then extended in one step to 1.7 Å. Refinement at this stage involved simulated annealing followed by *B*-factor refinement, with the extensive use of simulated annealing omit maps (Fig. 4b). The final model refined in X-PLOR contained residues 6–200 and 211 water molecules. This model was refined with REFMAC[19] (Table 1). The maximum-likelihood method in REFMAC lowered the *R*-values in the highest resolution shell (from 38.4 to 33.7% for R_{free} at 1.76–1.7 Å). All ϕ and ψ angles lie in the allowed regions of the Ramachandran plot, with 92% in the most favourable regions. Side-chain densities are well defined for all residues except 151–153 in a loop, which have *B*-factors >70 $Å^2$.

Figure preparation. Figures 1a, 2 and 3 were prepared using the program RIBBONS[30].

Received 27 May; accepted 3 July 1997.

1. Ljuggren, H. G. & Karre, D. In search of the "missing self": MHC molecules and NK cell recognition. *Immunol. Today* **11,** 237–244 (1990).
2. Lanier, L. L. Natural killer cells: from no receptors to too many. *Immunity* **6,** 371–378 (1997).
3. Long, E. O. *et al.* Killer cell inhibitory receptors: diversity, specificity, and function. *Immunol. Rev.* **155,** 135–144 (1997).
4. Fan, Q. R. *et al.* Direct binding of a soluble natural killer cell inhibitory receptor to a soluble human leukocyte antigen-Cw4 class I major histocompatibility complex molecule. *Proc. Natl Acad. Sci. USA* **93,** 7178–7183 (1996).
5. Wagtmann, N. *et al.* Molecular clones of the p58 natural killer cell receptor reveal Ig-related molecules with diversity in both the extra- and intracellular domains. *Immunity* **2,** 439–449 (1995).
6. Bork, P., Holm, L. & Sander, C. The immunoglobulin fold: structural classification, sequence patterns and common core. *J. Mol. Biol.* **242,** 309–320 (1994).
7. Kossiakoff, A. A. *et al.* Comparison of the intermediate complexes of human growth hormone bound to the human growth hormone and prolactin receptors. *Protein Sci.* **3,** 1697–1705 (1994).
8. Livnah, O. *et al.* Functional mimicry of a protein hormone by a peptide agonist: the EPO receptor complex at 2.8 Å. *Science* **273,** 464–471 (1996).
9. De Vos, A. M., Ultsch, M. & Kossiakoff, A. A. Human growth hormone and extracellular domain of its receptor: crystal structure of the complex. *Science* **255,** 306–312 (1992).
10. Somers, W., Ultsch, M., De Vos, A. M. & Kossiakoff, A. A. The X-ray structure of a growth hormone–prolactin receptor complex. *Nature* **372,** 478–481 (1994).
11. Walter, M. R. *et al.* Crystal structure of a complex between interferon-γ and its soluble high-affinity receptor. *Nature* **376,** 230–235 (1995).
12. Muller, Y. A., Ultsch, M. H., Kelly, R. F. & De Vos, A. M. Structure of the extracellular domain of human tissue factor: location of the factor VIIa binding site. *Biochemistry* **33,** 10864–10870 (1994).
13. Harlos, K. *et al.* Crystal structure of the extracellular region of human tissue factor. *Nature* **370,** 662–666 (1994).
14. Wang, J. *et al.* Atomic structure of a fragment of human D4 containing two immunoglobulin-like domains. *Nature* **348,** 411–418 (1990).
15. Ryu, S. *et al.* Crystal structure of an HIV-binding recombinant fragment of human CD4. *Nature* **348,** 419–426 (1990).
16. Jones, E. Y., Davis, S. J., Williams, A. F., Harlos, K. & Stuart, D. I. Crystal structure at 2.8 Å resolution of a soluble form of the cell adhesion molecule CD2. *Nature* **360,** 232–239 (1992).
17. Huber, A. H., Wang, Y. E., Bieber, A. J. & Bjorkman, P. J. Crystal structure of tandem type III fibronectin domains from *Drosophila* neuroglian at 2.0 Å. *Neuron* **12,** 717–731 (1994).
18. Bazan, J. F. Structural design and molecular evolution of a cytokine receptor family. *Proc. Natl Acad. Sci. USA* **87,** 6934–6938 (1990).
19. Collaborative computational project No. 4. The CCP4 suite: Programs for protein crystallography. *Acta Crystallogr. D* **50,** 760–776 (1994).
20. Winter, C. C. & Long, E. O. A single amino acid in the p58 killer cell inhibitory receptor controls the ability of NK cells to discriminate between the two groups of HLA-C allotypes. *J. Immunol.* **158,** 4026–4028 (1997).
21. Burshtyn, D. N. *et al.* Recruitment of tyrosine phosphatase HCP by the killer cell inhibitory receptor. *Immunity* **4,** 77–85 (1996).
22. Binstadt, B. A. *et al.* Sequential involvement of Lck and SHP-1 with MHC-recognizing receptors on NK cells inhibits FcR-initiated tyrosine kinase activation. *Immunity* **5,** 629–638 (1996).
23. Ihle, J. N., Witthuhn, B. A., Quelle, F. W., Yamamoto, K. & Silvennoinen, O. Signaling through the hematopoietic cytokine receptors. *Annu. Rev. Immunol.* **13,** 369–398 (1995).
24. Biassoni, R. *et al.* The human leukocyte antigen (HLA)-C-specific "activatory" or "inhibitory" natural killer cell receptors display highly homologous extracellular domains but differ in their transmembrane and intracytoplasmic portions. *J. Exp. Med.* **183,** 645–650 (1996).
25. Pende, D. *et al.* The natural killer cell receptor specific for HLA-A allotypes: a novel member of the p58/p70 family of inhibitory receptors that is characterized by three immunoglobulin-like domains and is expressed as a 140-kD disulfide-linked dimer. *J. Exp. Med.* **184,** 505–518 (1996).
26. Hendrickson, W. A. Determination of macromolecular structures from anomalous diffraction of synchrotron radiation. *Science* **254,** 51–58 (1991).
27. Ramakrishnan, V. & Biou, V. Treatment of MAD data as a special case of MIR. *Meth. Enzymol.* **276,** 538–557 (1996).
28. Otwinowski, Z. *Isomorphous Replacement and Anomalous Scattering* (Daresbury Laboratory, UK, 1991).
29. Brünger, A. T. *X-PLOR, Version 3.1: A System for X-ray and NMR* (Yale Univ. Press, New Haven, CT, 1992).
30. Carson, M. Ribbon models of macromolecules. *J. Mol. Graph.* **5,** 103–106 (1987).
31. Cromer, D. T. Calculation of anomalous scattering factors at arbitrary wavelengths. *J. Appl. Crystallogr.* **16,** 437 (1983).

Acknowledgements. We thank D. N. Garboczi, X. D. Zhang, P. Rosenthal, K. Smith and L. Chen for help with data collection; R. Hellmiss for preparing Fig. 1b; W. I. Weis and V. Ramakrishnan for discussion; Y. Liu for the program for calculating *f′* and *f″* values; W. Kossiakoff for the coordinates of the hPLR–hGH complex; Harvard microchemistry facility for mass spectroscopy; A. Haykov and R. Crouse for technical support; the staff at the Brookhaven X25 beamline and CHESS for assistance with data collection; and D. N. Garboczi for reading the manuscript. Q.R.F. is a recipient of an NSF predoctoral fellowship. L. M. is an associate and D. C. W. is an investigator of the Howard Hughes Medical Institute.

Correspondence and requests for materials should be addressed to D.C.W. (e-mail: wiley@crystal.harvard.edu). Coordinates will be deposited in the Brookhaven Data base and are available now from Q.R.F. (e-mail: fan@crystal.harvard.edu).

erratum

Neurotactin, a membrane-anchored chemokine upregulated in brain inflammation

Yang Pan, Clare Lloyd, Hong Zhou, Sylvia Dolich, Jim Deeds, Jose-Angel Gonzalo, Jim Vath, Mike Gosselin, Jingya Ma, Barry Dussault, Elizabeth Woolf, Geoff Alperin, Janice Culpepper, Jose Carlos Gutierrez-Ramos & David Gearing

Nature **387,** 611–617 (1997)

The sequence of neurotactin reported in this Letter is identical to that of fractalkine, a CX_3C membrane-bound chemokine reported in a Letter by J. F. Bazan *et al.* in *Nature* **385,** 640–644 (1997), published while the paper by Pan *et al.* was under consideration. A note to this effect in the paper by Pan *et al.* was inadvertently omitted by *Nature*. □

Nature © Macmillan Publishers Ltd 1997

Crystal structures of fragment D from human fibrinogen and its crosslinked counterpart from fibrin

Glen Spraggon*, Stephen J. Everse* & Russell F. Doolittle

Center for Molecular Genetics, University of California, San Diego, La Jolla, California 92093-0634, USA
** These authors contributed equally to this work.*

In blood coagulation, units of the protein fibrinogen pack together to form a fibrin clot, but a crystal structure for fibrinogen is needed to understand how this is achieved. The structure of a core fragment (fragment D) from human fibrinogen has now been determined to 2.9 Å resolution. The 86K three-chained structure consists of a coiled-coil region and two homologous globular entities oriented at approximately 130 degrees to each other. Additionally, the covalently bound dimer of fragment D, known as 'double-D', was isolated from human fibrin, crystallized in the presence of a Gly-Pro-Arg-Pro-amide peptide ligand, which simulates the donor polymerization site, and its structure solved by molecular replacement with the model of fragment D.

Fibrinogen units pack together to form a fibrin clot[1], but without a crystal structure it is difficult to understand how this is achieved. Fibrinogen is readily purified from blood plasma, but it is fragile, and efforts to crystallize the native molecule have so far been unsuccessful. But electron microscopy long ago revealed that fibrinogen has a trinodular structure[2], the distal globular entities of which were thought to be joined to a central domain by 'coiled coils'[3]. Biochemical characterization showed the molecule to be a covalent dimer composed of six polypeptide chains ($\alpha_2\beta_2\gamma_2$) linked by an extensive network of disulphide bonds, and enormous effort had to be expended to understand how the six chains were accommodated by the triglobular structure. It turns out that each of the two terminal globular domains contains the three non-identical chains ($\alpha\beta\gamma$), and that these are tethered together in the smaller central domain, which contains all six amino termini. The three-stranded connectors can be broken by proteases such as plasmin, generating two principal core fragments: a small fragment corresponding to the central domain (fragment E), and a set of larger fragments corresponding to terminal portions (fragments D). The two D fragments together account for half the mass of the native molecule. In contrast, fragment E, which is mostly composed of the two three-stranded connectors joined near their N termini, amounts to only 15% of the starting molecule. The remaining third of the protein is accounted for by the free-standing C-terminal two-thirds of the α-chains, which are readily removed by most proteases.

It has been presumed that both fragments D and E contain substantial portions of the severed 'coiled coil', the boundaries of which have been thought to be 'disulphide rings'[4]. Thus the three non-identical chains in each half of a fibrinogen molecule are interconnected by two sets of 'disulphide rings', which are distinguished by homologous braces of cysteines separated in each case by three residues.

Numerous biochemical and biophysical studies have been conducted on fragments derived from both fibrinogen and fibrin in an effort to understand the formation of fibrin clots and fibrinolysis. Briefly, clotting occurs when thrombin removes fibrinopeptides from the centrally located α-chain N termini, thereby exposing new N-terminal sequences known as 'knobs' (in the fragment E region). These spontaneously interact with 'holes' on the distal domains of other fibrinogen molecules (in the fragment D regions). Because the molecule is a dimer, oligomerization can proceed in either direction, the result being a two-molecule thick protofibril with a half-molecule staggered overlap. Peptides fashioned on the 'knob' sequences bind to fibrinogen, as well as to fragment D, and can effectively prevent polymerization[5]. It is because fragment D contains the 'hole' half of the knob–hole interaction that it is physiologically active as an inhibitor of fibrin formation.

Concomitantly, the polymerizing fibrin oligomers are reinforced by the thrombin-activated translutaminase known as factor XIII, which introduces γ-glutamyl-ε-amino-lysine isopeptide crosslinks between the carboxyl-segments of abutting γ-chains[6]. The protofibrils subsequently associate laterally to form first fibrils and then mature fibres, additional crosslinks slowly being added between the carboxyl regions of a small fraction of α-chains. When fibrin formed under crosslinking conditions is proteolysed, the core fragments released are E and crosslinked D ('double-D' or 'D-dimer')[7], as well as the unstable complex known as 'D_2E'[8].

Although a detailed atomic structure of fibrinogen has not yet been determined, combined electron microscopy and X-ray diffraction efforts have yielded an 18-Å structure for a protease-modified molecule[9], and recently a high-resolution X-ray structure has been reported for one of the two domains of M_r 30K that constitute the terminal globules[10]. We now report an X-ray structure at 2.9 Å for

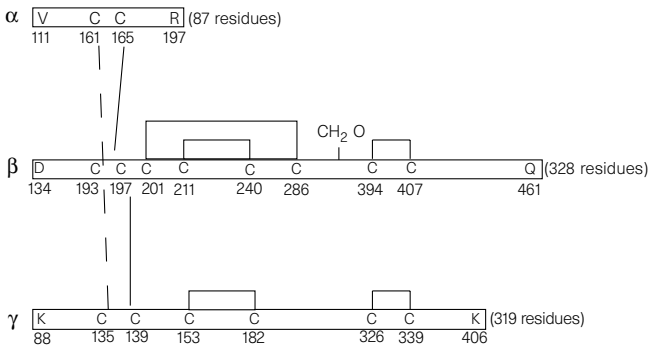

Figure 1 Schematic representation of the three polypeptide chains that compose human fibrinogen fragment D. The 16 cysteine residues are involved in three interchain and five intrachain disulphide bonds[14]. Residue numbering corresponds to native human fibrinogen, in which the α-chain runs from Alaα1 to Valα610, the β-chain from PCAβ1 to Glnβ461, and the γ-chain from Tyrγ1 to Valγ411.

Nature © Macmillan Publishers Ltd 1997

the 86K entity known as fragment D. It is composed of three disulphide-linked polypeptide chains ($\alpha'\beta'\gamma'$) and contains 734 amino-acid residues, the α', β' and γ' chains having 87, 328 and 319 residues, respectively (Fig. 1).

We have also isolated the factor XIII-crosslinked counterpart, double-D, from a carefully controlled proteolytic digest of human fibrin, and solved its structure by molecular replacement with the model of fragment D. Moreover, the double-D was co-crystallized with the ligand Gly-Pro-Arg-Pro-amide, which mimics the 'knobs' contributed by the fragment E portion of the knob–hole interaction[5]. As a result, the structure allows us to determine the three main events that occur during the initial stages of fibrin formation: the Gly-Pro-Arg knob–hole interaction; the D–D 'self-association'; and the whereabouts of the γ–γ crosslinks. Finally, given the locations of the surrogate 'knobs' and a general knowledge of the extent of the coiled coils and the dimensions of fragment E, we were able to construct a model of the fundamental fibrin monomer and the oligomeric protofibril.

Structure determination

The structure of fragment D was solved by the use of multiple isomorphous replacement and anomalous scattering (MIRAS) techniques, using gold, mercury and uranium derivatives. The initial MIRAS phases were improved by solvent flattening, after which tubes of electron density corresponding to the expected coiled coils could be discerned in a 6-Å map; a clear delineation of the entire monomer envelope by inspection was not possible, however. The matter was resolved by an envelope-skeletonization procedure (G.S., in preparation), which provided a preliminary mask that was subsequently used as a search model with the self-rotation angles to determine accurate non-crystallographic symmetry (n.c.s.) matrices for the structure. The initial mask was improved by correlation mapping, after which averaging was performed on the maps themselves, followed by limited phase extension to 3.5 Å. This strategy resulted in a considerably improved map that allowed almost an entire chain trace of the molecule to be made. After the initial trace was made, the quality of maps was improved by cross-averaging the native fragment-D map with that from a non-isomorphous crystal of fragment D and maps from double-D (below). During the model-building phase, we took advantage of the homologous nature of the β and γ globular domains, the better density in one or the other of these serving as a guide.

The structure was refined using a combination of positional, simulated annealing, and thermal parameter refinement, beginning from a crystallographic *R*-value of 52.1% at 2.9-Å resolution. This was followed by alternating cycles of manual refitting to SigmaA-weighted and cross-averaged maps. The model refinement was monitored closely by determining the free *R*-factor, and all weights were set on this basis. The model was refined with n.c.s. constraints throughout. In the latter stages of refinement, an anisotropy and bulk solvent correction were included. In the end, a model with good statistics at 2.9 Å emerged (Table 1); the conventional *R*-factor was 26.3% and the free *R*-factor 36.3%, with good stereochemistry as shown by Ramachandran plots. Only two residues involved in disulphide bonds fell into disallowed regions (Cys β407, Cys γ339). In total, 707 of the chemically expected 734 residues were positioned; the 27 absences were all situated at the termini: β134–147, α196–197, β461 and γ397–406. In the final stages of building and refinement, the electron density improved to the point where the single calcium atom[11] could be added to the γ-chain globular domain, as was a nominal sugar residue in the case of the β-chain[12].

The structure of the factor XIII-crosslinked double-D was determined by molecular replacement using an unrefined chain trace of native D as a model; all data in the resolution range 8–4 Å were used. The rotation search generated two peaks approximately 180 deg apart, both of which were subjected to two-dimensional translation searching. The correlation coefficients for the two solutions were 22.8% (4.8σ above the mean) and 24.9% (7.5σ above the mean), respectively; the corresponding *R*-factors were 52.9% and 52.4%. When one solution was fixed and the other searched for in the *y*-direction for the four origins of the $P2_1$ asymmetric unit, the correlation coefficient rose to 38.7% (the next highest solution was 26.3%) and the *R*-factor dropped to 48.4%. The electron density of the Gly-Pro-Arg-Pro-amide ligands was clearly evident in a $2|F_o| - |F_c|$ map.

The double-D structure was refined beginning from a crystallographic *R*-factor of 50.9% on all data between 8.0 and 2.9 Å resolution. This was followed by alternating cycles of manual refitting to $2|F_o| - |F_c|$ maps and refinement of atomic positions

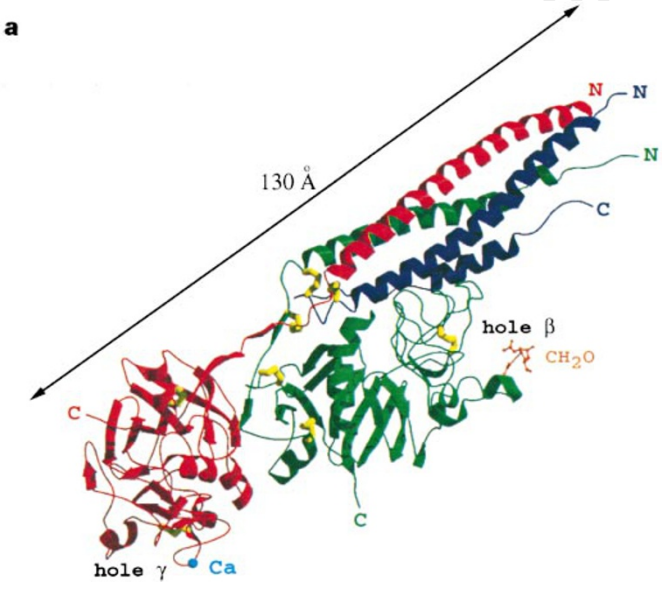

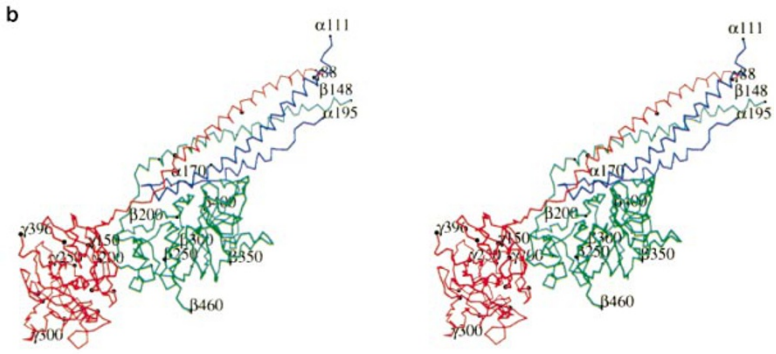

Figure 2 a, Ribbon representation of fragment D, showing the region of coiled coils and the globular β and γ domains. Colour scheme: blue, α-chain; green, β-chain; red, γ-chain; yellow, disulphide bonds. N and C denote amino and carboxy termini, respectively; Ca, calcium-binding site; CH_2O, carbohydrate cluster at Asnβ364; 'hole' denotes potential binding cavity. **b**, Stereo view of α-carbon trace of fragment D. Markers on chains are shown at 50-residue intervals.

Nature © Macmillan Publishers Ltd 1997

and *B*-factors. The final conventional *R*-factor was 24.1% and the free *R*-factor was 31.8% with good stereochemistry (Table 1). Refinement was monitored closely by the free *R*-factor, and all weights were determined on this basis. Initially, the model was refined with the use of n.c.s. constraints. In later stages of refinement, a restrained regime was adopted, warranted by a significant drop in the free *R*-factor upon application of weights of 100 kcal mol^{-1} imposed on all atoms related by n.c.s. In the very last stages, an anisotropic *B*-factor and bulk solvent correction were applied, and all data from 30 to 2.9 Å were included.

General description of fragment D structure

The overall architecture of the 130-Å long fragment is plough-shaped, beginning with the three-stranded coiled-coil region and a double-back fourth helical segment of α-chain, and continuing on to two prominent globular regions corresponding to the carboxyl halves of the β- and γ-chains, respectively (Fig. 2). The two domains are orientated relative to each other at about 130 deg. The β domain is folded back close to the coiled coil; the γ domain extends onwards to a distal position.

The remnant coiled coil in fragment D consists of residues Valα111 to Serα160 (50 residues), Aspβ134 to Tyrβ192 (59 residues), and Lysγ88 to Glnγ134 (47 residues). The N-terminal 14 residues of the β-chain, which are mostly unmatched in the other chains (Fig. 1), are disordered and do not appear in the model. The packing of the three chains in the coiled coil is canonical, with most of the non-polar side chains directed inward. The clockwise arrangement of the three chains in fragment D, as seen from the N termini, is α–γ–β.

The fourth helix in the bundle corresponds to residues Serα166 to Proα195. It nestles in the groove between the α- and β-chains on the face of the coiled coil opposite to the γ-chain with its non-polar side chains directed inward. The situation is reminiscent of the influenza haemagglutinin HA_2 structure, which also has a hairpin helix associated with a coiled coil[13].

The disulphide connections linking the three chains are different from what was expected. Previous chemical determinations[14] had established that Cysβ193 is linked to Cysα165, but the other two disulphides could not be assigned at that time. It was predicted on symmetry grounds, however, that they would connect Cysα161 to Cysγ139 and Cysγ135 to Cysβ197. Instead, the X-ray structure reveals that, whereas Cysβ193 is indeed connected to Cysα165, the other two connections are between Cysα161 and Cysγ135, and Cysγ139 and Cysβ197. The asymmetric arrangement is in keeping with the unexpected reversal of direction for the α chain.

Homologous globular domains

The β- and γ-chains form a short two-stranded parallel β-sheet (strands denoted '0' in Fig. 3a) as they proceed away from the disulphide junction before adopting separate courses that orientate

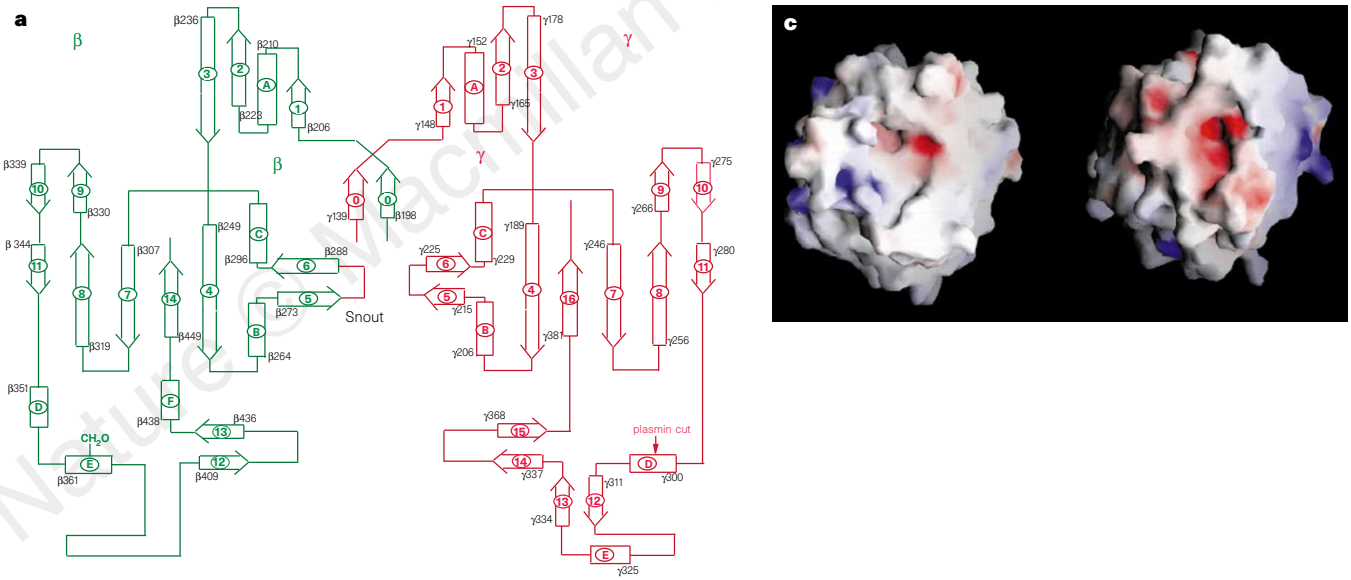

Figure 3 a, Topology of β-chain (green) and γ-chain (red) C-terminal domains. The first residue in each segment of secondary structure is numbered. **b**, Stereo depiction of superposed Cα backbone structures from globular portions of β-chains (green) and γ-chains (red); the numbers on the strands and letters on the helices correspond to the secondary structure designations in Fig. 4. **c**, GRASP representation of binding cavities of β-chains (left) and γ-chains (right) showing charge distribution; red, negatively charged; blue, positively charged[47]. Domains have been reorientated to show equivalent projections.

Nature © Macmillan Publishers Ltd 1997

Nature © Macmillan Publishers Ltd 1997

them at about 130 deg to each other. Beyond that, there is only one interaction between the two domains, an antiparallel β-sheet composed of residues Asnβ202–Valβ205 and Glyγ216–Serγ219. Each of the homologous domains consists of two small subdomains, at the N- and C-terminal ends, respectively, and a central domain with a 5-stranded antiparallel β-sheet (Fig. 3a). A large extended helix is interrupted by a snout-like region. In the β-chain, the snout-like region protrudes further than in the γ-chain, the result of an eight-residue insertion that includes Cysβ286, which is bonded to Cysβ201 near the disulphide junction.

In both chains, the C-terminal subdomain is composed of three extended loops that form the cavity expected for a ligand-binding site. As anticipated, the calcium-binding site in the γ domain is contiguous to the binding cavity (Fig. 2), as is the protease-sensitive bond at Lysγ302. One unexpected feature of the structure is that residues Lysγ381–Aspγ390 in one case, and Lysβ453–Pheβ458, in the other, fold back from the C-terminal subdomain and form a central β strand in the main domain.

For the most part, our structure is in good agreement with a recently reported structure of the γ-chain globular domain[10]. In that

Table 1 Statistics for data collection, phase determination and refinement

	Fragment D Space group: $P2_1$ Unit cell: a = 107.72, b = 48.08, c = 167.56, β = 105.70° Asymmetric unit: 2 molecules							Double D Space group: $P2_1$ Unit cell: a = 93.82, b = 95.5, c = 113.76, β = 96.08° Asymmetric unit: 1 molecule
	Native	$KAuCl_4$	$KAuCl_4$ (anomalous)		HgI_4	HgI_4 (anomalous)	$UO_2(NO_3)_2$	
Beam	UCSD	Daresbury	Daresbury	Daresbury	SSRL	Daresbury	SSRL	BNL
Detector	MW	Mar	Mar	Mar	Mar	Mar	Mar	Mar
λ (Å)	1.54	0.88	0.88	0.88	1.08	0.88	1.08	1.02
d_{min} (Å)		2.9	2.9	2.9	3.3	2.9	3.3	2.9
Number of crystals		9	1	1	1	1	1	5
Observations (N)		318,238	141,315	141,315	140,160	90,389	110,282	244,386
Unique reflections (N)		35,552	27,080	27,074	24,106	19,596	23,548	40,637
Mean redundancy		8.95	5.2	5.2	5.8	4.6	4.7	6.0
Data coverage (%)		87.1	71	71	92	60	81	88.8
R_{sym} (I) (%)*		14.5	9.5	9.5	18.2	12.5	13.2	19.2
Mean isomorphous difference (%)†			18.0			26.1		14.6
MIR analysis								
d_{min} (Å)			4.0	4.0	5.0	5.0	4.5	
Heavy-atom sites/asymmetric unit			4	4	1	1	2	
Phasing power‡			1.72	1.71	0.83	1.27	1.16	
R_{cullis}§			0.607		0.693		0.658	
Mean overall figure of merit‖		0.496						

Refinement	Native D model: 707 residues (5,712 atoms)		DD Model: 1,414 residues (11,391 atoms)	
d-spacings (Å)	30.0–2.9	3σ cutoff	30.0–2.9	3σ cutoff
R-value¶ (%)	26.3	23.1	24.1	21.8
Free R-value	36.3	32.5	31.8	29.2
r.m.s.d. bonds (Å)	0.011		0.010	
r.m.s.d. angles (°)	1.63		1.54	
r.m.s.d. B values (Å^2)	4.7		4.3	
Average B value	25.00		30.81	

* $R_{sym} = \Sigma |I - \langle I \rangle| / \Sigma |I|$.
† Mean isomorphous difference $= \Sigma ||F_{(PH)}| - |F_{(P)}|| / \Sigma |F_{(P)}|$, where $F_{(P)}$ is the protein structure factor amplitude and $F_{(PH)}$ is the heavy-atom derivative structure factor amplitude.
‡ Phasing power = r.m.s. $\Sigma |F_H| / E$, where F_H is the calculated heavy-atom structure factor amplitude and E is the lack of closure error.
§ $R_{cullis} = \Sigma ||F_{(PH)} \pm F_{(P)}| - |F_{H(calc)}|| / \Sigma |F_{(PH)} \pm F_{(P)}|$ for centric reflections only.
‖ Mean figure of merit $= \Sigma |F_{(hkl)best}| / F_{(hkl)}$.
¶ Crystallographic R-value $= \Sigma ||F_{(Obs)}| - |F_{(Calc)}|| / \Sigma |F_{(Obs)}|$ with 95% of the native data for refinement. Free R-value: R-value based on 5% of the native data withheld from refinement.
MW, multiwire detector; Mar, Mar imaging plate; SSRL, Stanford Synchrotron Radiation Laboratory.

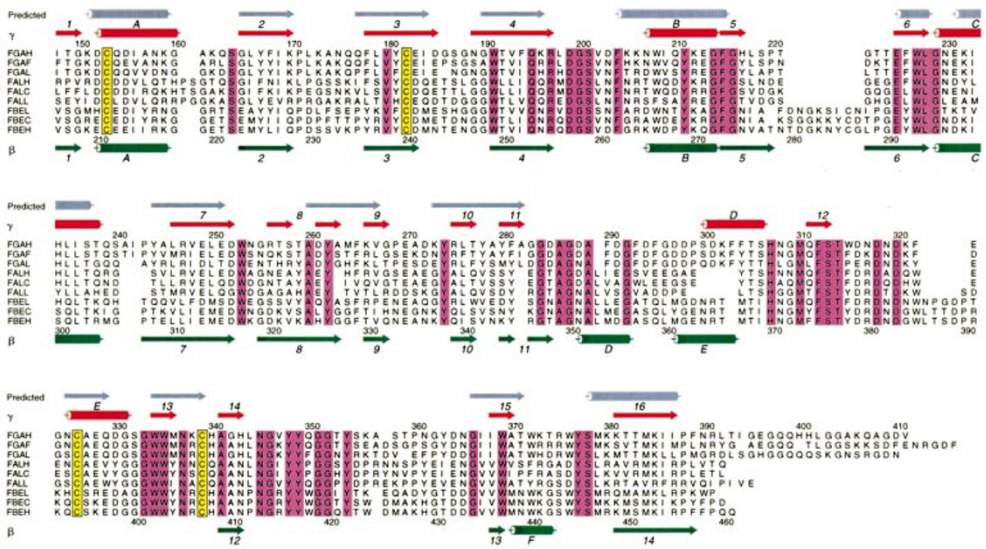

Figure 4 Multiple alignment of carboxyl domains of fibrinogen β (FBE)- and γ (FGA)-chains from various species (H, human; F, frog; C, chicken; L, lamprey). Also included are related domains from minor forms of (FAL) chains[49,50]. The observed secondary structures of the human γ- and β-chains, with their human numbering, are shown above and below the alignment, respectively; α-helices are denoted with capital letters and β strands with numbers. A longstanding secondary-structure prediction[15] is shown in grey at the top.

Nature © Macmillan Publishers Ltd 1997

study, some ambiguity was reported for the C-terminal segment, different crystal forms giving rise to different conformations. Similarly, in our native fragment-D structure we were not able to model in the last 10 residues at the C-terminal end of the γ-chain. It was possible, however, to trace the shorter β-chain almost all the way to the C-terminal Glnβ461 in the native fragment D. For the most part, the β- and γ-chain folds are very similar (Fig. 3b), the root-mean-square (r.m.s.) distance being 1.42 Å for 220 aligned residues.

There are a few important differences, however, including two short helices in the β-chain and a short helix and some additional β structure in the γ-chain (Figs 3a and 4). Also, the β domain has a five-residue insertion that, as forecast[15], disrupts the calcium-binding site. In addition, the β-chain has a carbohydrate cluster at Asnβ364 (Fig. 1), which is reported to be of the biantennary type[12]. The non-protein density in this region is disordered, and only a nominal sugar was incorporated in the model.

As noted above, both the β and γ domains have large cavities that are well disposed for binding peptides (Fig. 3c). Equilibrium dialysis studies[5] have shown that both sites should bind Gly-Pro-Arg-peptides, but only the β site should bind Gly-His-Arg-peptides, which correspond to the thrombin-exposed N termini of β-chains. The binding cavity in the γ-chain has much more electronegative quality than does the β-chain equivalent (Fig. 3c). It may also be important that the single sugar residue incorporated in the model is positioned at the very mouth of the β-chain cavity. In the γ-chain, the structures in good accord with the biochemistry, Tyrγ363 being inside the γ-chain binding cavity, as expected on the basis of affinity-labelling studies[16].

A search of reported three-dimensional structures did not show any significant resemblances to known proteins, a result in accord with the recent report on the γ-chain carboxyl domain[10]. At the sequence level, however, the β and γ globular domains are known to be homologous with numerous other C-terminal domains found in animal extracellular proteins, including tenascins, restrictins, ficolin and calcium-dependent lectins found in both vertebrates and invertebrates. Previously, an effort had been made to predict the secondary structure of these domains on the basis of a diverse multiple alignment and various biochemical considerations[15]. If a three-state criterion is used (α-helix, β-sheet or other), then 81% of the residues were assigned correctly (Fig. 4). As anticipated, the accuracy of the prediction was greater in the N-terminal half of the domain, the looser carboxyl-segment being more ambiguous. Another prediction with much the same results has recently appeared[17].

Structure of double-D

In general, the structure of the double-D closely resembles that of two molecules of fragment D butted end-to-end, conformational changes as such being modest. There are some slight changes in the positions of the helices in the coiled coil near their N termini, and the ligand-binding pocket in the γ-chain does undergo some readjustment. In this regard, the binding of the Gly-Pro-Arg 'knobs' involves both electrostatic interactions and hydrogen bonding, the α-amino group being juxtaposed between residues Aspγ364 and Aspγ330, and the guanidino group of the arginine lying between the carboxyl group fo Aspγ364 and Glnγ329 (Fig. 5a, b). Variant human fibrinogens with defective polymerization have been reported for all three of these sites[18,19]. Fibrinogen Matsumoto I has Aspγ364 mutated to His, fibrinogens Kyoto III and Milano have Aspγ330 mutated to Tyr and Val, respectively, and fibrinogen Nagoya has Glnγ329 changed to Arg. Some other reported variants are involved less directly by disrupting the network of hydrogen bonds involving important residues. Additionally, the loop containing residue Tyrγ363, which is known to be within the binding cavity on the basis of affinity-labelling experiments[16], has moved relative to its position in native D. The r.m.s.d. for the Cα atoms of the segment Lysγ356–Asnγ365 is 1.54 Å.

The two γ-chain binding cavities are on the same side of the fibrin dimer, which has a 'sidedness' or dorsal–ventral aspect (Fig. 6a, b). The fragment E region of fibrinogen, which includes the two Gly-Pro-Arg 'knobs' in the native molecule and is intrinsically dimeric, must straddle the junction on the side diametrically opposite the crosslinks. Because the two α-chains contributing the Gly-Pro-Arg 'knobs' (residues Glyα17–Argα19) are joined by a disulphide bond only nine residues away (Cysα28) that necessarily falls on the two-fold axis of native fibrinogen, it was possible to position a model mask of the fragment E as it would be in the 'D_2E' complex and the beginning protofibril (Fig. 6c, d). In this regard, a crude model of fragment E was constructed by first applying a rotation of 180 deg

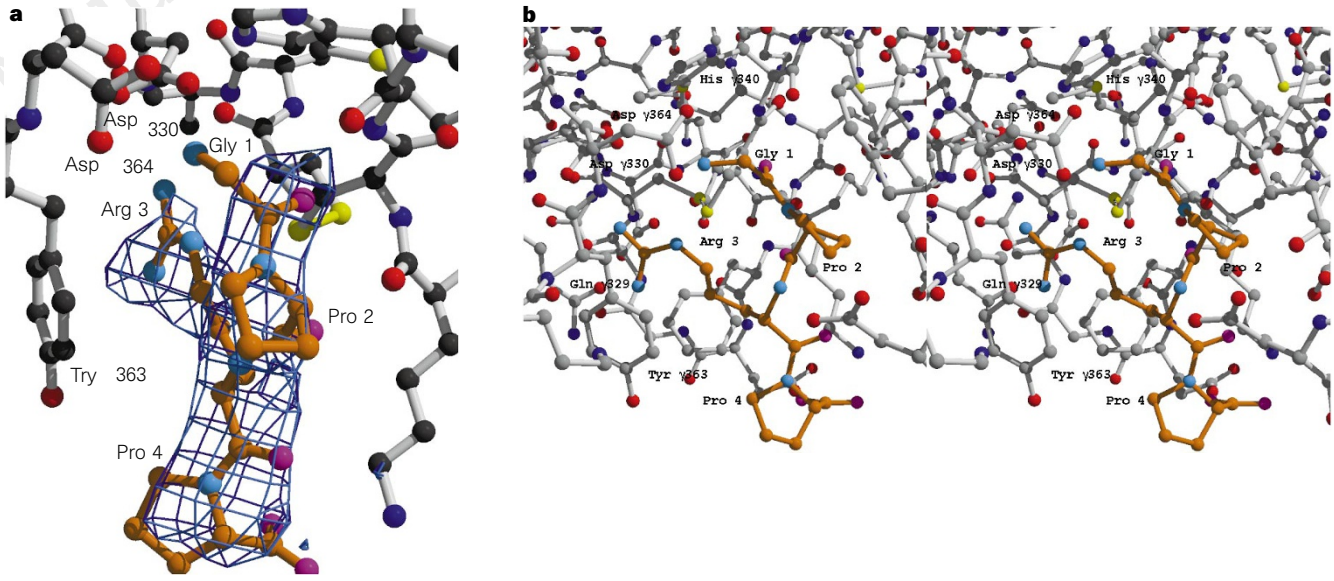

Figure 5 a, Electron-density omit map showing peptide ligand Gly-Pro-Arg-Pro-amide bound to γ-chain binding site in double-D as calculated with $|F_o| - |F_c|$ coefficients and phases from the refined model contoured at 2.2σ. The ligand model was not included in the F_c calculation. **b**, Stereoscopic view of ball-and-stick model showing ligand position in binding site. Residue numbering corresponds to native human fibrinogen.

Nature © Macmillan Publishers Ltd 1997

along the long axis of double-D, followed by translations of the half-stagger distance (225 Å) along this same axis and the width of double-D in a perpendicular direction. The coiled coil of this reoriented double-D was extended backwards by the correct number of residues to reach the disulphide ring in fragment E (for example, Cysα45–Cysα49). It was then a simple matter to draw the short connections to the disulphide dyad (Cysα28–Cysα28) and on to the experimentally determined 'knobs' in the untranslated double-D. The other half of fragment E was constructed by applying the n.c.s. operators of the double-D structure. The symmetrical model for fragment E is in the form of a double dog-leg, the result of being anchored on the two ligands on the one hand, and the extensions to meet the coiled coils in D on the other (Fig. 6c). A model of the protofibril can be constructed by repeated application of the operations and their inverse (Fig. 6d).

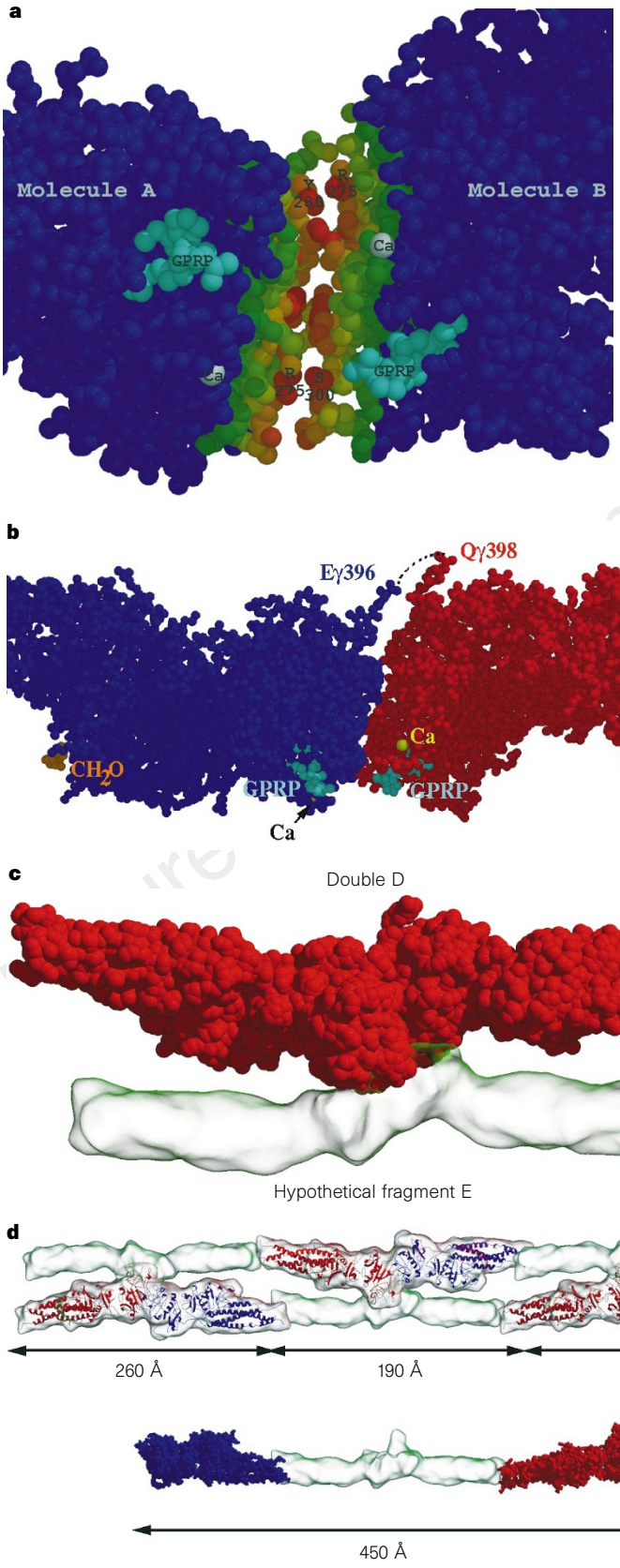

Figure 6 Four views across the D–D interface as seen from increasing distance. **a**, Close-up showing structural details of end-to-end abutment of fragments D in double-D: R, Argγ275; Y, Tyrγ280; S, Serγ300; Ca, calcium atoms; GPRP, Gly-Pro-Arg-Pro-amide ligands. The residues at the interface are coloured according to their nearest distances to residues on the other side of the crevice, red being shortest and greater distances shading toward green. **b**, More distant view showing Gluγ396 of molecule A and Glnγ398 of molecule B connected by a broken line denoting crosslink; CH_2O, carbohydrate. **c**, Even more distant view of fibrin double-D with hypothetical fragment E domain rooted on the two Gly-Pro-Arg ligands and straddling the interface of abutting D domains. **d**, Very distant view showing three molecules of double-D connected by hypothetical structures corresponding to full-sized fragments E and connecting segments to show required packing in protofibrils. A fibrin monomer made from two halves of the double-D structure and the hypothetical fragment E is shown at the bottom.

End-to-end association of fibrin monomers.

The end-to-end association of joined fragments D occurs in a staggered fashion such that a significant but not maximal amount of surface area is occluded between the extremeties (Fig. 6a). Accessibility measurements indicate that approximately 750 $Å^2$ of surface is lost as a result of the association, a modest contribution to the free energy of polymerization[20]. There is a distinct crevice between the associated ends that probably contains some solvent. The offset nature of the association relative to the major molecular axis requires an asymmetric set of interactions between the adjacent fibrin units. Of particular interest is residue Argγ275, one of the most frequently reported mutations in polymerization-defective human fibrinogens[19]. In native fragment D, this residue has its guanidino group within hydrogen-bonding distance of the carboxyl

Nature © Macmillan Publishers Ltd 1997

group of Aspγ272. The two corresponding arginine residues in double-D are not significantly moved in that regard, but two different intermolecular interactions are now evident. In molecule A, the guanidino group is within hydrogen-bonding distance of the hydroxyl group of Serγ300 on molecule B. The equivalent group on molecule B is opposite Tyrγ280 on molecule A.

Although calcium has been reported to improve fibrin formation in some mutant fibrinogens[19], there is no evidence that calcium is involved in the end-to-end association, as revealed by the structure, and the effect must either be the result of maintaining the general structural integrity at the nearby calcium-binding site (Fig. 6a, b), or the calcium is contributing to a later stage in polymerization.

It has long been recognized that fibrin formation involves an end-to-end interaction independent of either the Gly-Pro-Arg-dependent knob–hole interaction or the γ–γ crosslinks, and it has been predicted[21], on the basis of the variant human fibrinogen denoted Tokyo II, that Argγ275 must be involved in that end-to-end interaction. The X-ray structure verifies that prediction exactly.

Crosslinks

The reciprocally linked γ-chain carboxyl segments are not visible in the electron-density maps and must have some mobility despite being connected from one unit to another. The logic of their whereabouts derives from the observations that the two fragments D are chemically linked to each other, as is readily shown on SDS gels, and that the X-ray structure shows that the two fragments D are situated end-to-end. The ϵ-amino γ-glutamyl crosslinks, which are known[6] to involve Glnγ398 and Lysγ406, join two molecules that are end-to-end. Because of the offset nature of the end-to-end interaction, the two different γ-chain carboxyl segments must have different conformations (Fig. 6b). This may explain why different investigators have reported different conformations for this region[10,22]. In our maps, the electron density was discernible up to Gluγ396 in molecule A, and up to Glnγ398, the crosslink acceptor residue, in molecule B (Fig. 6b). The Cα–Cα distance between them is 17 Å, perhaps slightly too far for a simple helical connector of the 10 residues (15 Å) needed to reach the molecule A donor at Lysγ406, but definitely too short for a simple antiparallel β strand (34 Å). In any case, the connections are on the opposite side of the joined units from where the knob–hole interactions occur.

There has long been debate over whether the γ–γ crosslinks connect neighbouring molecules in an end-to-end manner (longitudinal)[23] or side by side (transverse)[24]. The crystal structure now demonstrates that they are connected end to end. Nonetheless, the crosslinked segments are so exposed and readily accessible to factor XIII that it should be possible for additional crosslinks to be formed with other protofibrils, which may explain reports of crosslinked trimers and tetramers[25]. The peripheral location of the crosslinks also shows how the extended γ-chain known as γ′, reported to be a binding site for factor XIII[26], would remain external after the association of fibrin monomers and would itself be crosslinked.

Other physiological considerations

As well as providing details about how the individual units are packed in the protofibril, these structures allow us to investigate subsequent interactions in fibrin formation. They also allow us to consider other important differences between fibrinogen and fibrin, particularly the physiological matter of how various cells and macromolecules distinguish between these two entities.

The reversal of the α-chain at the fragment-D disulphide ring came as a surprise, but in retrospect it may make good biological sense for several reasons. First, the known plasmid cut-points in the region Lysα206–Argα239 are near the cuts that sever the coiled coil. Second, the direction of the chain in this region is consistent with reports that the C-terminal domains of α-chains are located in the central parts of the molecule[27]. Third, the model in which the intramolecular associations of α-chain C-terminal domains are broken during the polymerization process and reassociated in an intermolecular mode[28] might explain how certain features of the coiled coil could be exposed in fibrin but not in fibrinogen.

As an example, the sequence Lysα151–Argα159, which is part of the coiled coil immediately adjacent to the disulphide ring, has been reported to activate tissue-type plasminogen activator in fibrin but not in fibrinogen[29]. In fragment D, this region of the α-chain is closed off on one side by the β globular domain, on two others by the β- and γ-helices, and on its 'frontside' by the fourth helix. Measures of solvent accessibility showed the segment to be totally buried. Given the proposal that the α-chain carboxyl region moves away from the parent molecule during polymerization[28], it might seem reasonable that the fourth helix could be pulled away from the coiled coil and expose the masked residues, but we observed no significant difference in this region in the double-D fragment isolated from fibrin. One possibility is that the fourth helix is pulled away, but then snaps back into the groove after plasmin clipping, in which case the double-D would not be expected to be an activator of t-PA, but it has been reported to be active[30]. For the moment, the important difference between fibrin and fibrinogen with regard to biologically active groups remains unresolved.

A recent report shows that the Gly-Pro-Arg-Pro-amide ligand binds to the 30K γ-chain domain[31]. □

Methods

Protein preparation and crystallization. Fragment D was prepared from trypsin-digested human fibrinogen[32] made from bloodbank plasma. N-terminal sequencing revealed an almost homogeneous protein with Valα111, Aspβ134 and Metγ89, with a small amount of Lysγ88 present. We thank T. Takagi of Tohoku University for determining the sequences. Sialic acids were removed by digestion with neuraminidase; some preparations were purified further by DEAE-chromatography. Crystals were grown at room temperature from sitting drops with wells containing 16–19% PEG 3350, 50 mM Tris, pH 7.5–8.5, 2 mM NaN_3 and 50–133 mM $CaCl_2$. Macroseeding was used to obtain large crystals for diffraction studies[33].

The double-D fragment was prepared directly from lysed crosslinked fibrin generated by adding bovine thrombin (0.1 U ml^{-1}) to human fibrinogen (7.5 mg ml^{-1}, 0.15 M NaCl) in the presence of 10 mM $CaCl_2$ and 5 mM cysteine. The clot formed within 2 min. After 18 min, 0.05 original volumes of a trypsin solution (1 mg ml^{-1}) was added and the digestion allowed to proceed for 4 h at room temperature, at which point 0.05 original volumes of a soybean trypsin inhibitor solution (3 mg ml^{-1}) was added to stop further digestion. The solution was passed over a Sephadex G-150 gel filtration column (2.5 × 85 cm, 4 °C) that had been equilibrated with 1 M NaBr, 0.05 M sodium acetate, pH 5.3. The leading peak was pooled and precipitated by adding 0.33 volume saturated ammonium sulphate. The suspension was chilled on ice for 15 min before centrifugation, after which the supernatant was discarded and the pellet stored frozen at −20 °C until needed. Unreduced preparations gave essentially single bands with an apparent M_r of 170K on SDS gels. Precipitates were dissolved in minimal volumes of 0.05 M Tris buffer, pH 7.5, 0.005 M $CaCl_2$, quick-dialysed against that same buffer, adjusted to 10 mg ml^{-1}, and set for crystallization.

Crystals were obtained under similar conditions to those that were effective for native fragment D[33], except that the $CaCl_2$ concentration was reduced to 10 mM and the Gly-Pro-Arg-Pro-amide was set at 5 mM. Sitting drops were maintained at room temperature; the exact well conditions were: 13–14% PEG, 50 mM Tris, pH 7.0, 10 mM $CaCl_2$, 5 mM Gly-Pro-Arg-Pro-amide, 1 mM NaN_3.

Crystallographic methods and data processing. Initial data collection and heavy-metal screening was conducted at room temperature on a Rigaku RU200 rotating anode generator and two area detectors (San Diego Multiwire Systems). Programs included with the San Diego Modelling System were used to scale and merge these data. The higher-resolution data used in the final model of fragment D were collected at the Daresbury synchrotron and Stanford Synchrotron Radiation Laboratory (Table 1). The double-D data were collected at the National Synchrotron Light Source, Brookhaven National Laboratory. Data collected on image plates were scaled with Denzo and ScalePack[34].

Nature © Macmillan Publishers Ltd 1997

Fragment D crystals soaked in 1 mM $KAuCl_4$ for 6 days yielded reproducible gold derivatives as identified by peaks on the Harker section of a standard difference Patterson. The Harker section from the difference Patterson map contained four distinct peaks, but the maps could not be solved by conventional Patterson-solving programs or manually[35]. Accordingly, six different data sets for gold derivatives were collected and the resulting isomorphous Patterson maps averaged together in Patterson space. This procedure enhanced the pattern on the Harker section and revealed that the four peaks were actually cross-peaks for two sets of atoms lying coplanar with each other at right angles to the crystallographic *y*-axis. Two additional heavy-metal derivatives (uranium and mercury) were subsequently identified by difference Fourier techniques. The two-site second derivative was identified from crystals soaked in 1 mM $UO_2(NO_3)_2$ for 10 days, as well as the third derivative from crystals soaked in 1 mM HgI_4 (HgI_2 + excess KI) for 6 days.

Heavy-atom refinement and phasing was carried out with the PHASES package[36]. The positioning of the heavy atoms and the poor quality of the initial solvent-flattened mask cast doubt on the exact boundaries of the molecular envelope. Great improvement was attained by a simple procedure of envelope-skeletonization with a program called Envder (G.S., manuscript in preparation). In brief, a search is made of the asymmetric unit (solvent envelope) for the largest sphere that can be contained within the envelope without penetrating solvent and not contained wholly within other spheres. A seed sphere is then set and other spheres connected to it by determining the mutual overlap. If the overlap exceeds a user-defined value, the spheres are considered to be connected. The operation is repeated until the number of monomers (two in this case) in the asymmetric unit is reached. The centre of mass of the monomers can be determined from this, and so, in combination with self-rotation angles, can an approximate translation vector. The molecular envelope is then used to refine the n.c.s. matrices against the correlation coefficient.

The envelope was further improved by correlation mapping[37] and averaging and limited phase extension with the RAVE package[38] and DM[35]. Model building was performed with O[39], and molecular replacement was done with X-PLOR[40], as were the structure refinements. SigmaA-weighting was performed as described[41]. The structure-homology search was performed with DALI[42]. Figures were created from the following programs: MOLSCRIPT[43,44]; RASTER3D[45,46]; GRASP[47]; ALSCRIPT[48].

Received 20 June; accepted 8 August 1997.

1. Bailey, K., Astbury, W. T. & Rudall, K. M. Fibrinogen and fibrin as members of the keratin–myosin group. *Nature* **151,** 716–717 (1943).
2. Hall, C. E. & Slayter, H. S. The fibrinogen molecule: its size, shape and mode of polymerization. *J. Biophys. Biochem. Cytol.* **5,** 11–15 (1959).
3. Cohen, C. Invited discussion at 1960 Symposium on Protein Structure. *J. Polymer Sci.* **49,** 144–145 (1961).
4. Doolittle, R. F., Cassman, K. G., Cottrell, B. A., Friezner, S. J. & Takagi, T. Amino acid sequence studies on the α-chain of human fibrinogen. The covalent structure of the α-chain portion of fragment D. *Biochemistry* **16,** 1710–1710 (1977).
5. Laudano, A. P. & Doolittle, R. F. Studies on synthetic peptides that bind to fibrinogen and prevent fibrin polymerization. Structural requirements, numbers of binding sites and species differences. *Biochemistry* **19,** 1013–1019 (1980).
6. Chen, R. & Doolittle, R. F. γ–γ Crosslinking sites in human and bovine fibrin. *Biochemistry* **10,** 4486–4491 (1971).
7. Pizzo, S. V., Schwartz, M. L., Hill, R. L. & McKee, P. A. The effects of plasmin on the subunit structure of human fibrin. *J. Biol. Chem.* **248,** 4574–4583 (1973).
8. Hudry-Clergeon, G., Patural, L. & Suscillon, M. Identification d'un complexe (D-D) E dans les produits de dégradation de la fibrine bovine stabilisee par le facteur XIII. *Pathol. Biol.* **22** (suppl.)**,** 47–52 (1974).
9. Rao, S. P. S. *et al.* Fibrinogen structure in projection at 18 Å resolution electron density by co-ordinated cryo-electron microscopy and X-ray crystallography. *J. Mol. Biol.* **222,** 89–98 (1992).
10. Yee, V. C. *et al.* Crystal structure of a 30 kDa C-terminal fragment from the γ chain of human fibrinogen. *Structure* **5,** 125–138 (1997).
11. Dang, C. V., Ebert, R. F. & Bell, W. R. Localization of a fibrinogen calcium binding site between γ-subunit positions 311 and 336 by terbium fluorescence. *J. Biol. Chem.* **260,** 9713–9717 (1985).
12. Townsend, R. R. *et al.* Carbohydrate structure of human fibrinogen. *J. Biol. Chem.* **257,** 9704–9710 (1982).
13. Bullough, P. A., Hughson, F. M., Skehel, J. J. & Wiley, D. C. Structure of the influenza haemagglutinin at the pH of membrane fusion. *Nature* **371,** 37–43 (1994).
14. Bouma, H. III, Takagi, T. & Doolittle, R. F. The arrangement of disulfide bonds in fragment D from human fibrinogen. *Thromb. Res.* **13,** 557–562 (1978).
15. Doolittle, R. F. A detailed consideration of a principal domain of vertebrate fibrinogen and its relatives. *Protein Sci.* **1,** 1563–1577 (1992).
16. Yamazumi, K. & Doolittle, R. F. Photoaffinity labeling of the primary fibrin polymerization site: Localization of the label to tyrosine γ-chain Tyr-363. *Proc. Natl Acad. Sci. USA* **89,** 2893–2896 (1992).
17. Gerloff, D. E., Cohen, F. E. & Benner, S. A. A predicted consensus structure for the C terminus of the β and γ chains of fibrinogen. *Proteins Struct. Funct. Genet.* **27,** 279–289 (1997).
18. Okumura, N. *et al.* Fibrinogen Matsumoto I: a γ364 Asp ≫ His (GAT to AT) substitution associated with defective fibrin polymerization. *Thromb. Haemost.* **75,** 887–891 (1996).
19. Ebert, R. .F. (ed.) *1994 Index of Variant Human Fibrinogens* (CRC Press, Boca Raton, FL, 1994).
20. Janin, J., Miller, S. & Chothia, C. Surface, subunit interfaces and interior of oligomeric proteins. *J. Mol. Biol.* **204,** 155–164 (1988).
21. Mosesson, M. W. *et al.* The role of fibrinogen D domain intermolecular associaiton sites in the polymerization of fibrin and fibrinogen Tokyo II (γ275 Arg to Cys). *J. Clin. Invest.* **96,** 1053–1058 (1995).
22. Donahue, J. P., Patel, H., Anderson, W. F. & Hawiger, J. Three-dimensional structure of the platelet integrin recognition segment of the fibrinogen γ chain obtained by carrier protein-driven crystallization. *Proc. Natl Acad. Sci. USA* **92,** 12178–12182 (1994).
23. Weisel, J. W., Francis, C. W., Nagaswami, C. & Marder, V. J. Determination of the topology of factor XIIIa-induced fibrin γ-chain cross-links by electron microscopy of ligated fragments. *J. Biol. Chem.* **268,** 26618–26624 (1993).
24. Mosesson, M. W., Siebenlist, K. R., Hainfeld, J. F. & Wall, J. S. The covalent structure of factor XIIIa crosslinked fibrinogen fibrils. *J. Struct. Biol.* **115,** 88–101 (1995).
25. Mosesson, M. W., Siebenlist, K. R., Amrani, D. L. & DiOrio, J. P. Identification of covalently linked trimeric and tetrameric D domains in crosslinked fibrin. *Proc. Natl Acad. Sci. USA* **86,** 1113–1117 (1989).
26. Siebenlist, K. R., Meh, D. A. & Mosesson, M. W. Plasma factor XIII binds specifically to fibrinogen molecules containing γ′ chains. *Biochemistry* **35,** 10448–10453 (1996).
27. Mosesson, M. W., Hainfeld, J., Wall, J. & Haschemeyer, R. H. Identification and mass analysis of human fibrinogen molecules and their domains by scanning transmission electron microscopy. *J. Mol. Biol.* **153,** 695–718 (1981).
28. Veklich, Y. I., Gorkun, O. V., Medved, L. V., Nieuvenhuizen, W. & Weisel, J. W. Carboxyl-terminal portions of the α chains of fibrinogen and fibrin. Localization by electron microscopy and the effects of isolated αC fragments on polymerization. *J. Biol. Chem.* **268,** 13577–13585 (1993).
29. Schielen, W. J. G., Adams, H. P. H. M., Voskuilen, M., Tesser, G. J. & Nieuwenhuizen, W. Structural requirements of position Aα-157 in fibrinogen for the fibrin-induced rate enhancement of the activation of plasminogen by tissue-type plasminogen activator. *Biochem. J.* **276,** 655–659 (1991).
30. Nieuwenhuizen, W., Vermond, A., Voskuilen, M., Traas, D. W. & Verheijen, J. H. Identification of a site in fibrin(ogen) which is involved in the acceleration of plasminogen activation by tissue-type plasminogen activator. *Biochim. Biophys. Acta* **748,** 86–92 (1983).
31. Pratt, K. P. *et al.* The primary fibrin polymerization pocket: three-dimensional structure of a 30-kDa C-terminal γ chain fragment complexed with the peptide Gly-Pro-Arg-Pro. *Proc. Natl Acad. Sci. USA* **94,** 7176–7181 (1997).
32. Mihalyi, E. & Godfrey, J. E. Digestion of fibrinogen by trypsin. II. Characterization of the large fragment obtained. *Biochim. Biophys. Acta* **67,** 90–103 (1963).
33. Everse, S. J., Pelletier, H. & Doolittle, R. F. Crystallization of fragment D from human fibrinogen. *Protein Sci.* **4,** 1013–1016 (1995).
34. Otwinowski, Z. & Minor, W. Processing of X-ray diffraction data collected in oscillation mode. *Methods Enzymol.* **276,** 307–326 (1997).
35. Collaborative Computing Project Number 4 The CCP4 suite: Programs for Protein Crystallography Version 3.1. *Acta Crystallogr. D* **50,** 760–763 (1994).
36. Furey, W. & Swaminathan, S. Phases 95: A program package for processing and analyzing diffraction data from macromolecules. *Methods Enzymol.* (in the press).
37. Stein, P. E. *et al.* The crystal structure of pertussis toxin. *Structure* **2,** 45–57 (1994).
38. Kleywegt, G. J. & Jones, T. A. From first map to final model. Joint CCP4 and ESF-EACBM. *Newslett. Protein Crystallogr.* **31,** 59–66 (1994).
39. Jones, T. A., Zou, J.-Y., Cowan, S. W. & Kjeldgaard, M. Improved methods for building protein models in electron density maps and the location of errors in these models. *Acta Crystallogr. A* **47,** 110–119 (1991).
40. Brunger, A. T. *X-PLOR. Version 3.1. A System for X-ray Crystallography and NMR* (Yale Univ. Press, New Haven, CT, 1992).
41. Read, R. J. Improved Fourier coefficients for maps using phases from partial structures with errors. *Acta Crystallogr. A* **42,** 140–149 (1986).
42. Holm, L. & Sander, C. Protein structure comparison by alignment of distance matrices. *J. Mol. Biol.* **233,** 123–138 (1993).
43. Kraulis, P. J. MOLSCRIPT: a program to produce both detailed and schematic plots of protein structures. *J. Appl. Crystallogr.* **24,** 946–950 (1991).
44. Esnouf, R. M. An extensively modified version of Molscript which includes greatly enhanced colouring capabilities. *J. Mol. Graphics* **15,** 133–138 (1997).
45. Bacon, D. J. & Anderson, W. F. A fast algorithm for rendering space-filling molecule pictures. *J. Mol. Graphics* **6,** 219–220 (1988).
46. Merritt, E. A. & Murphy, M. E. P. Raster3D verison 2.0: a program for photorealistic molecular graphics. *Acta Crystallogr. D* **50,** 869–873 (1994).
47. Nicholls, A., Sharp, K. & Honig, B. Protein folding and association: insights from the interfacial and thermodynamic properties of hydrocarbons. *Proteins Struct. Funct. Genet.* **11,** 281–296 (1991).
48. Barton, G. J. ALSCRIPT: a tool to format multiple sequence alignments. *Protein Eng.* **6,** 37–40 (1993).
49. Pan, Y. & Doolittle, R. F. cDNA sequence of a second fibrinogen α chain in lamprey: an archetypal version alignable with full-length β and γ chains. *Proc. Natl Acad. Sci. USA* **89,** 2066–2070 (1992).
50. Fu, Y., Cao, Y., Hertzberg, K. M. & Grieninger, G. Fibrinogen α genes: conservation of bipartite transcripts and carboxy-terminal-extended α subunits in vertebrates. *Genomics* **30,** 71–76 (1995).

Acknowledgements. We thank J. Kraut for the use of his X-ray faciities; M. Sawaya for his time; H. Pelletier for help in establishing the initial crystallization conditions; D. Stuart for assistance; N. Xuong and J. Noel for access to equipment; R. Sweet at the Brookhaven National Laboratory for assistance; G. Walter for encouragement; and M. Riley and L. Veerapandian for technical assistance. This work was supported by an NIH grant and an American Heart Association postdoctoral fellowship to S.J.E.

Correspondence and requests for materials should be addressed to R.D. (e-mail:rdoolittle@ucsd.edu). Coordinates have been deposited in the Brookhaven Protein Data Bank (accession nos: fragment D, 1FZA; double-D, 1FZB).

Nature © Macmillan Publishers Ltd 1997